Polymer chain dynamics in Newtonian and viscoelastic turbulent channel flows

V. K. Gupta, R. Sureshkumar, and B. Khomami
Department of Chemical Engineering, Washington University, St. Louis, Missouri 63130

(Received 21 March 2003; accepted 20 January 2004; published online 5 April 2004)

Polymer chain dynamics in Newtonian and viscoelastic turbulent channel flows are examined by Brownian dynamics simulations utilizing FENE and FENE–P [finitely extensible nonlinear elastic(–Peterlin)] dumbbell models. The chain extension is predicted by using an algorithm that combines the two-step semi-implicit predictor–corrector scheme for the evaluation of dumbbell trajectories with the direct numerical simulation of turbulent flow field. The influence of maximum extensibility of the polymer chain, b, the friction Reynolds number, Re_τ, and friction Weissenberg number, We_τ, on the chain dynamics in the viscous sublayer, buffer layer, and turbulent core is examined. For a given value of b, the average chain extension, $\langle|\mathbf{Q}|\rangle$, approaches an asymptotic value with increasing We_τ. For given values of We_τ and the friction Reynolds number, Re_τ, $\langle|\mathbf{Q}|\rangle/b$ decreases although $\langle|\mathbf{Q}|\rangle$ itself increases with increasing b. Significant qualitative and quantitative differences exist between the predictions obtained using the FENE and FENE–P models. Specifically, $\langle|\mathbf{Q}|\rangle$ values predicted by the FENE–P model are greater than those predicted by the FENE model for given We_τ and b. The normalized probability distribution function (pdf) for $\langle|\mathbf{Q}|\rangle$ predicted by the two models also shows differences. Violated states, i.e., configurations with $|\mathbf{Q}| > \sqrt{b}$, are seen for the FENE–P model while such states are not seen for the case of FENE model. Despite these differences, the quantitative differences between the predictions of the two models for $\langle\mathbf{QQ}\rangle$ in the viscous sublayer and the buffer layer can be practically eliminated by suitable renormalization of the maximum extensibility parameter. This renormalization also reduces the disparity between the FENE and FENE–P model predictions for the shear stress and transient extensional viscosity. Since mean chain extension and transient extensional behavior play a significant role in drag reduction (DR) such renormalization procedures could be used to improve the accuracy of continuum-level model predictions of DR. Comparison of simulation results obtained for $\mathrm{Re}_\tau=125$ and 180 shows that the dependence of pdf for $\langle|\mathbf{Q}|\rangle$ on We_τ and the renormalization proposed are not strongly influenced by Re_τ. However, the fraction of highly extended states is larger for $\mathrm{Re}_\tau=180$ while the states with low to moderate extension are smaller. Consequently $\langle\mathbf{QQ}\rangle$ increases only marginally with increasing Re_τ. © *2004 American Institute of Physics.* [DOI: 10.1063/1.1687415]

I. INTRODUCTION

The addition of small amounts of soluble high molecular weight polymers to inertia-dominated wall bounded flows not only affects their instability characteristics[1–8] but also reduces the turbulent drag.[9–14] It has been observed experimentally that even a very small amount [$O(100)$ ppm] of polymer additives in a flow can reduce drag up to 70%.[15] This has stimulated tremendous research effort. In the literature there are a large number of papers devoted to the experimental study of the wall layer structures in drag reducing flows. Several experimental observations have been made which indicate that the polymers modify the turbulence structures[15–24] within the buffer layer which is the most active region in wall bounded flows. These changes include increase in the dimensionless transverse spacing of the low-speed streaks within the buffer layer and reduction in the strength of the streamwise vortices.[25–29] In an attempt to investigate the effects of polymer extensibility and relaxation on the onset and the extent of drag reduction (DR), rheological studies were conducted on drag-reducing polymer systems.[30–34] Based on these experimental observations the proposed mechanisms of drag reduction rely on the extensional viscosity characterizing the enhanced fluid resistance to extensional motions[9,10,30–34] or relaxation time characterizing the elastic memory effects.[35–42] However, the extent to which either of these factors, i.e., chain relaxation and extensional thickening, contribute to drag reduction is unclear. Part of the difficulty lies in the fact that it has not yet been possible to obtain experimentally all the kinematic variables in drag reduced flows that provide information on vorticity and kinetic energy transport. Moreover, experimental visualization of polymer chain configurations in turbulent flows has not been possible. Consequently, experimental data for the coupling between polymer conformation and kinematics do not exist. However, in order to obtain information on polymer configuration-flow coupling that is central to drag reduction, one has to resort to direct numerical simulations (DNS) of viscoelastic turbulent flows.

The development of accurate and efficient spectral meth-

ods for viscoelastic turbulent flow simulation and their implementation on high performance computers have made it possible to investigate turbulent drag reduction in dilute polymer solutions.[43–49] Sureshkumar *et al.*[46] carried out DNS of the turbulent channel flow of a dilute polymer solution from first principles using kinetic theory based constitutive equation for the polymer. They modeled polymer chains as finitely extensible nonlinear elastic–Peterlin (FENE–P) dumbbells. In this model, the viscoelastic stress is related to the departure of the conformation tensor, $\tilde{\mathbf{c}}$, characterizing the ensemble average second moment of the polymer chain end-to-end distance vector. Their simulation results showed excellent qualitative agreement with experimental findings. In particular, they observed a decrease in the streamwise vorticity fluctuations and an increase in the average spacing between the streamwise streaks of low speed fluid within the buffer layer. They also demonstrated that the extent of drag reduction depends on the maximum average chain extensibility and the friction Weissenberg number, We_τ, defined as the ratio of the fluid relaxation time to the wall time scale ν_0/u_τ^2 where ν_0 is the zero shear kinematic viscosity of the fluid and u_τ is the friction velocity.[47] It has also been shown through continuum-level modeling that maximum chain stretch occurs on the surface of axial vortices and polymer stretch is correlated with the sweep and ejection cycles.[50–52]

Although many of the salient features of turbulent drag reduction were captured by the DNS studies,[46–48] details regarding the specifics of polymer chain orientation and its coupling to the kinematics have not been extensively explored. Since the DNS studies[46–49] are based on continuum level models the details of polymer configuration are described only in the ensemble-averaged sense. From the point of view of developing mechanistic ideas that can aid the development of simpler models of DR, it is desirable to obtain details of the polymer chain length and orientation distribution and how they depend on chain extensibility, the Weissenberg number and the location (i.e., viscous sublayer, buffer layer, or turbulent core) in the flow.

To date all investigations of chain dynamics using kinetic theory based models such as FENE, FENE–PM, and FENE chain have been limited to turbulent channel flow of a *Newtonian fluid*.[53] Although these studies have been limited to Newtonian kinematics, they have demonstrated that the mean chain extension are qualitatively and nearly quantitatively similar implying that the internal modes, i.e., degrees of freedom arising from a multibead spring model, do not play a very significant role in determining the extent of drag reduction.[54] Consequently, single segment dumbbell-based models can be utilized to explore the role of kinematics, chain extensibility and relaxation time on the distribution of chain extension and orientation in the flow. In this work we perform Brownian dynamics simulation (BDS) by utilizing FENE and FENE–P dumbbell models in drag reducing viscoelastic turbulent channel flow[46–49] for a wide range of extensibility and We_τ values to obtain detailed statistical information on chain dynamics. For comparison purposes BDS is also performed for Newtonian kinematics as well. The results obtained for the FENE and FENE–P models are also used to seek renormalization procedures for the maximum extensibility parameter in the FENE–P model. The paper is organized as follows. In Sec. II we present the governing equations and dimensionless parameters. Section III deals with the numerical method used to solve these equations. Section IV contains results and discussions. Conclusions are presented in Sec. V.

II. GOVERNING EQUATIONS

For the channel Poiseuille flow considered in this study, we choose the x axis as the mean flow direction, i.e., the direction of the constant, externally imposed, pressure gradient and the y and the z axes as the wall-normal and spanwise directions, respectively. We denote zero-shear kinematic viscosity as ν_0, defined as the ratio of total zero-shear viscosity μ_0, to the density of the polymer solution ρ. We use the friction velocity, defined as $U_\tau=\sqrt{\tau_w/\rho}$, as the velocity scale, where τ_w represents the shear stress at the wall, ν_0/U_τ as the length scale, and ν_0/U_τ^2 as the time scale. Using these scales the dimensionless equations for the conservation of momentum and mass become

$$\frac{\partial\tilde{\mathbf{v}}}{\partial t}+\tilde{\mathbf{v}}\cdot\nabla\tilde{\mathbf{v}}=-\nabla\tilde{p}+[\beta\nabla^2\tilde{\mathbf{v}}+(1-\beta)\nabla\cdot\tilde{\mathbf{T}}]+\frac{1}{\mathrm{Re}_\tau}\mathbf{e}_x, \tag{1}$$

$$\nabla\cdot\tilde{\mathbf{v}}=0, \tag{2}$$

where $\tilde{\mathbf{v}}$, $\tilde{p}$, and $\tilde{\mathbf{T}}$ denote the velocity, the excess pressure and the viscoelastic contribution to the total stress, respectively. The pressure is scaled by the wall shear stress τ_w. The last term in Eq. (1) represents the constant, mean pressure drop per unit length across the channel which in the dimensionless units used here is represented by the inverse of the friction Reynolds number $\mathrm{Re}_\tau\equiv hU_\tau/\nu_0$, where h is the channel half-width. The parameter β appearing in Eq. (1) represents the ratio of the solvent (μ_s) to the total zero-shear rate solution viscosity (μ_0). Finally, note that the viscoelastic stress tensor, $\tilde{\mathbf{T}}$ is made dimensionless using a viscous stress scaling, i.e., $\mu_{p0}U_\tau^2/\nu_0$, where $\mu_{p0}=\mu_0-\mu_s$ is the polymer contribution to the total zero-shear solution viscosity.

The system of equations (1) and (2) is supplemented by either selecting a closed form constitutive equation for the viscoelastic stress contribution or by evaluating the viscoelastic stress contribution as an appropriate expectation from an ensemble of polymer trajectories evaluated via BDS as described in Secs. II A and II B below.

A. Continuum-level constitutive equation

The closed form constitutive equation used is the FENE–P (finitely extensible nonlinear elastic–Peterlin) dumbbell model. The choice has been motivated by the fact that prior DNS simulations with this model have been able to qualitatively describe the DR phenomenon and the accompanying flow modifications.[46–49] In this model, a polymer chain is represented by a dumbbell consisting of two beads representing the hydrodynamic resistance connected by a finitely extensible entropic spring. The viscoelastic stress $\tilde{\mathbf{T}}$ is related to the departure of the conformation tensor $\tilde{\mathbf{c}}$, charac-

terizing the average second moment of the polymer chain end-to-end distance vector, from its equilibrium unit isotropic tensor state **1**, as

$$\tilde{\mathbf{T}}=\frac{\tilde{f}\tilde{\mathbf{c}}-\mathbf{1}}{\mathrm{We}_\tau}, \tag{3}$$

where $\mathrm{We}_\tau=\lambda U_\tau^2/\nu_0$ is the Weissenberg number, λ is the polymer relaxation time, and

$$\tilde{f}=\frac{L^2-3}{L^2-\mathrm{trace}(\tilde{\mathbf{c}})} \tag{4}$$

where L^2 is the square of the dimensionless (average) maximum extensibility, i.e., $\mathrm{trace}(\tilde{\mathbf{c}})\leqslant L^2$. Note that $\tilde{\mathbf{c}}$ and L^2 are made dimensionless with respect to kT/H^*, where k, T, and H^* denote the Boltzmann constant, the absolute temperature, and the Hookean dumbbell spring constant, respectively.

The evolution equation for the conformation tensor $\tilde{\mathbf{c}}$ is given by[37,55,56]

$$\frac{\partial\tilde{\mathbf{c}}}{\partial t}+\tilde{\mathbf{v}}\cdot(\nabla\tilde{\mathbf{c}})-[\tilde{\mathbf{c}}\cdot(\nabla\tilde{\mathbf{v}})+(\nabla\tilde{\mathbf{v}})^T\cdot\tilde{\mathbf{c}}]=-\frac{\tilde{f}\tilde{\mathbf{c}}-\mathbf{1}}{\mathrm{We}_\tau}. \tag{5}$$

Equations (1)–(5) along with the no-slip boundary conditions for the velocity on the channel walls, constitute the governing equations for the viscoelastic channel flow which are subsequently solved numerically.

B. Stochastic description of polymer dynamics

Kinetic theory based models used in this work are the FENE and the stochastic description of the FENE–P dumbbell models. Both models consist of elastic dumbbells having two Brownian beads attached by an entropic spring. The difference between the two lies only in the choice of the spring force. For the FENE dumbbell, the nonlinear spring force law takes the form[56]

$$\mathbf{F}^c=\frac{H^*\mathbf{Q}}{1-\left(\frac{Q}{Q_0}\right)^2}, \tag{6}$$

whereas for the FENE–P dumbbell,[56]

$$\mathbf{F}^c=\frac{H^*\mathbf{Q}}{1-\frac{\langle Q^2\rangle}{Q_0^2}}. \tag{7}$$

In the above equations, $\mathbf{F}^c$ is the spring force, $\mathbf{Q}$ is the connector vector between the beads, H^* is the spring constant, Q is the length of the connector, Q_0 is the maximum extensibility of the spring, and the angular brackets denote ensemble averaging. In both the models, the dumbbell connector vector $\mathbf{Q}$ satisfies the following stochastic differential equation:[57]

$$d\mathbf{Q}(t)=\left[\kappa(t)\cdot\mathbf{Q}(t)-\frac{1}{2\,\mathrm{We}}\tilde{\mathbf{F}}^c\right]dt+\sqrt{\frac{1}{\mathrm{We}}}d\mathbf{W}(t), \tag{8}$$

where κ is the transpose of the velocity gradient (i.e., $\kappa\equiv\nabla\mathbf{v}^T$), $\mathrm{We}=\lambda\langle U\rangle/h$ is the Weissenberg number, λ is the relaxation time of the polymer, $\langle U\rangle$ is the mean centerline velocity in the channel, and $d\mathbf{W}(t)$ is the Wiener process which accounts for the Brownian force experienced by the beads. The Wiener process is represented mathematically by a Gaussian random vector with zero mean and variance dt. In the above equation, $\mathbf{Q}$ has been made dimensionless by $\sqrt{kT/H^*}$, the equilibrium length of a (linear) Hookean dumbbell. Hence the dimensionless spring force can be written as $\tilde{\mathbf{F}}^c=\mathbf{Q}/(1-Q^2/b)$ for FENE dumbbells where $b=(H^*Q_0^2)/kT$ is the square of the dimensionless maximum extensibility, i.e., $\mathrm{trace}\langle\mathbf{QQ}\rangle\leqslant b$ and $\tilde{\mathbf{F}}^c=\mathbf{Q}/(1-\langle Q^2\rangle/L^2)$ for FENE–P dumbbells where $L^2=(H^*Q_0^2)/kT$ is the square of the dimensionless maximum extensibility for FENE–P dumbbells.

Equations (1), (2), and (8) combined with the force law given by either (6) or (7) along with the no-slip $\tilde{\mathbf{v}}=0$ boundary conditions for the velocity on the channel walls, constitute the governing equations for the viscoelastic channel flow.

The force law in the FENE–P model constrains the average square extensibility of the dumbbell to be less than the square of the contour length. Clearly in flows where the polymer end to end distribution function is broad [shear flows at $\mathrm{We}\sim O(100)$] or there are a large population of extended states (extensional flows) this constraint is not adequate since a large number of chains will have lengths higher than the chain contour length (i.e., violated states).[58–60] Moreover, the contribution of the extended states to the average polymer stress is considerable. Considering the stochastic nature of the flow kinematics in a turbulent channel flow, the existence of highly extended states particularly during ejection and sweep events is highly probable.

Although the continuum and stochastic FENE–P model are equivalent, the continuum formulation only provides information regarding the conformation tensor. Hence, one cannot ascertain the number of violated states and their contribution to the overall stress. Thus, we have performed the multiscale FENE–P simulations.

Clearly performing multiscale simulations with the FENE model that excludes the possibility of having a state with length greater than the contour length would allow one to assess the influence of violated states on the percentage drag reduction predicted by the FENE–P model. However, performing hi-fidelity multiscale simulations with the FENE model is beyond current supercomputing power. The rationale behind this statement is discussed below.

To date two basic approaches for multiscale simulation of dilute polymeric solutions have been developed. The first approach is CONNFFESSIT[61] and the second is the Brownian configuration fields (BCF).[62,63] In what follows the applicability of these techniques to stochastic flows such as turbulent flows will be discussed.

BCF: This technique relies on spatial correlation of kinetic species within a field. Hence, the evolution of each field is evaluated using standard Eulerian techniques.[62,63] This approach is very attractive as it can be easily interfaced with standard Eulerian approaches such as finite element,

finite difference, finite volume, and spectral formulations for solving conservation equations. In addition, it provides absolute spatial variance reduction and various variance reduction techniques have been developed to improve temporal accuracy.[63,64] Hence, this is a very efficient technique for multiscale simulations for deterministic flows. However, the fact that in this approach the kinetic species are spatially correlated limits its use to deterministic flows. Therefore, one cannot use this technique to perform multiscale simulations of turbulent channel flows.

CONNFFESSIT: This technique relies on tracking individual polymer chains. This Lagrangian approach requires very large ensembles as well as very accurate particle trajectories to provide accurate results. Hence, it is extremely CPU and memory intensive. To reduce the CPU and memory requirements of this technique, new approaches have been developed that use few kinetic species (i.e., dumbbell, etc.) in a particle (used in the tracking algorithm) to provide spatial variance reduction.[65,66] Although the most advanced version of the CONNFFESSIT technique is not as computationally efficient as the BCF method, they are the methods of choice for performing multiscale simulation of turbulent channel flows. However, a number of issues need to be addressed before one can perform high-fidelity simulations. These issues are outlined below.

Particle trajectory: Although backward Eulerian particle tracking techniques have been developed for deterministic flows their application to stochastic flows is not a trivial task. Any deviation of the particle trajectory from the true particle trajectory will give rise to large errors in the polymer dynamics because the chains will sample an incorrect velocity gradient. Indeed, this could give rise to excessive center of mass diffusion of the polymer in a very similar fashion as the use of excessive artificial diffusion in purely Eulerian formulations. This is particularly important during highly localized dynamical events such as ejections and sweeps. In fact, any error in tracking the particles could give rise to a negative value of the trace of the conformation tensor.

Ensemble size: In order to obtain reasonable chain dynamics in the stochastic flow (see Sec. III B) a large ensembel size is required [i.e., $O(10^3)$]. With a reasonable mesh size for a spectral simulation ($64\times65\times64$) at most 100 kinetic species can be tracked with the current supercomputing power. Clearly this is insufficient for obtaining a reasonable distribution function, particularly since many trajectories will violate the condition that the trace of the conformation tensor should be positive.

Considering the above issues we have adopted the following strategy for performing multiscale simulations. Specifically, Eqs. (1)–(5), i.e., the continuum-level governing equations for the FENE–P fluid are solved self-consistently to obtain $\tilde{\mathbf{v}}$, $\tilde{p}$, $\tilde{\mathbf{c}}$ for drag-reduced flows for $6.25 \leqslant \mathrm{We}_\tau \leqslant 125$. The velocity field from these simulations are used to perform BDS [using Eq. (8)] of FENE and FENE–P dumbbells to obtain the evolution of $\mathbf{Q}$. Once $\mathbf{Q}(t)$ have been evaluated for a number of trajectories, the viscoelastic stress contribution can be obtained by using Kramer's expression[56]

$$\tau_p = \frac{1-\beta}{\mathrm{We}^*}(\langle \tilde{\mathbf{F}}^c \mathbf{Q}\rangle - \langle \tilde{\mathbf{F}}^c \mathbf{Q}\rangle_{\mathrm{eqbm}}), \tag{9}$$

where $\langle \tilde{\mathbf{F}}^c \mathbf{Q}\rangle_{\mathrm{eqbm}} = \mathbf{1}$, the unit tensor and $\mathrm{We}^* = \mathrm{We}/(1+5/b)$. We note that the Weissenberg number We defined above is related to the friction Weissenberg number (based on wall scales) as $\mathrm{We}_\tau = \mathrm{We}\,\mathrm{Re}_\tau^2/\mathrm{Re}_m$ where Re_m denotes the Reynolds number based on the mean flow rate.

Although the above computational strategy will produce fully self-consistent results for the FENE–P model, the kinematics used in the FENE simulations is an approximation of the true kinematics. At a first glance one might conclude that this approach would not produce accurate predictions of the chain dynamics. This is true if one is interested in the short time dynamics of the macromolecules, however, we are interested in the average chain extension over several eddy turnover times as this has been shown to be the quantity that determines the extent of drag reduction.[47] Towards this end our assumption should be very reasonable as prior DNS studies with various kinematic theory dumbbell based models (e.g., FENE–P, Giesekus, and Oldroyd-B) have shown that time averaged kinematics such as the average velocity and rms velocity fluctuations predictions are very similar for this class of models provided that they are compared at a given value of average chain extension.[47]

III. NUMERICAL METHOD

The numerical algorithm used for the time-integration of Eqs. (1)–(5) was developed by Sureshkumar and Beris[49] in an earlier work, based on a semi-implicit, time-splitting, spectral algorithm.[45,46] In this section we describe the two-step semi-implicit predictor–corrector (SIPC) scheme for the timeintegration of Eq. (8).[57] This algorithm circumvents configurations in the unphysical range since in this algorithm the spring-force law is treated implicitly. In this algorithm given the solution $\mathbf{Q}^n$ at time $t = n\,\delta t$, the solution $\mathbf{Q}^{n+1}$ at the next time step $t = (n+1)\,\delta t$, is obtained as follows.

Predictor-step,

$$\overline{\mathbf{Q}}(t^{n+1}) = \mathbf{Q}(t^n) + \left[\kappa(t^n)\cdot\mathbf{Q}(t^n) - \frac{1}{2}\frac{1}{\mathrm{We}}\tilde{\mathbf{F}}^c(t^n)\right]\delta t + \sqrt{\frac{1}{\mathrm{We}}}\,\mathrm{d}\mathbf{W}(t^n). \tag{10}$$

Corrector-step,

$$\mathbf{Q}(t^{n+1}) = \mathbf{Q}(t^n) + \frac{1}{2}[\kappa(t^{n+1})\cdot\overline{\mathbf{Q}}(t^{n+1}) + \kappa(t^n)\cdot\mathbf{Q}(t^n)]\,\delta t - \frac{1}{2}\left[\frac{1}{2\,\mathrm{We}}\tilde{\mathbf{F}}^c(t^{n+1}) + \frac{1}{2\,\mathrm{We}}\tilde{\mathbf{F}}^c(t^n)\right]\delta t + \sqrt{\frac{1}{\mathrm{We}}}\,\mathrm{d}\mathbf{W}(t^n). \tag{11}$$

For the FENE model the second step upon rearrangement, results in the following cubic equation for the magnitude of $\mathbf{Q}$:

TABLE I. Weissenberg number vs percentage drag reduction.

We_τ	0	6.25	12.5	25	37.5	50	62.5	75	87.5	100	125
% DR	0	0.8	5.6	18.2	24.5	29.6	32.7	33.6	34.5	35.9	37.0

TABLE II. Convergence with respect to ensemble size and time step.

trace$\langle \mathbf{QQ} \rangle$	N_s	δt
369.75 ± 7.55	1000	0.002
371.67 ± 5.36	2000	0.002
367.17 ± 5.32	2000	0.006

$$|\mathbf{Q}|^3 - \mathbf{R}*|\mathbf{Q}|^2 - b\left(1 + \frac{\delta t}{4\,\mathrm{We}}\right)|\mathbf{Q}| + b\mathbf{R} = 0, \tag{12}$$

where $\mathbf{R}$ is the magnitude of the right-hand side vector in Eq. (11). This equation has one unique root between 0 and $\sqrt{b}$, and thus by choosing this root, we ensure that $|\mathbf{Q}|$ is always less than or equal to $\sqrt{b}$.

For the FENE–P model due to the presence of the term $\langle \mathbf{QQ} \rangle$ which depends on $\mathbf{Q}$ values of all the dumbbells, the second step upon rearrangement results in a set of highly nonlinear system of equations. In order to solve this set of equations, similar to our earlier studies on dynamics of FENE chains,[67] we split the term $\langle \mathbf{QQ} \rangle^{n+1}$ into $\langle \mathbf{QQ} \rangle^{n+1}$ for the dumbbell for which $|\mathbf{Q}|$ is being solved and $\langle \mathbf{QQ} \rangle^{n}$ for the rest of the dumbbells. This again leads to a cubic equation of the form (12) which can be easily solved. Once every $\mathbf{Q}^{n+1}$ is known, the residual ϵ is calculated as the difference between the solutions $\mathbf{Q}$ and $\mathbf{Q}^{n+1}$ according to the following equation:

$$\epsilon = \sqrt{\sum_{i=1}^{N_s} (\mathbf{Q}_i^{n+1} - \overline{\mathbf{Q}}_i)^2}, \tag{13}$$

where N_s is the number of dumbbells. The corrector step is repeated until numerical convergence is achieved.

Once all the $\mathbf{Q}$'s have been evaluated, the polymeric stress τ_p is obtained by using Eq. (9).

A. Simulation conditions

Recent computations by Housiadas and Beris[68] have shown that the extent of DR is relatively insensitive to $\mathrm{Re}_\tau (125 \leqslant \mathrm{Re}_\tau \leqslant 590)$ at a fixed We_τ and L^2. Hence, we have performed simulations at two Re_τ, namely, 125 and 180. Extensive parametric studies are performed only for $\mathrm{Re}_\tau = 125$. Due to the significant increase in CPU time and memory, simulations performed for $\mathrm{Re}_\tau = 180$ are primarily used to test the influence of flow inertia on the results (see Sec. IV C). The simulations are carried out in a unit cell of dimensions $10h \times 2h \times 5h$ for $\mathrm{Re}_\tau = 125$ and $6.944h \times 2h \times 3.472h$ for $\mathrm{Re}_\tau = 180$ in the x, y, and z directions, respectively. The streamwise (x) dimension of the unit cell is chosen to be the largest to capture the elongated quasistreamwise vortical structures. The simulations reported in this

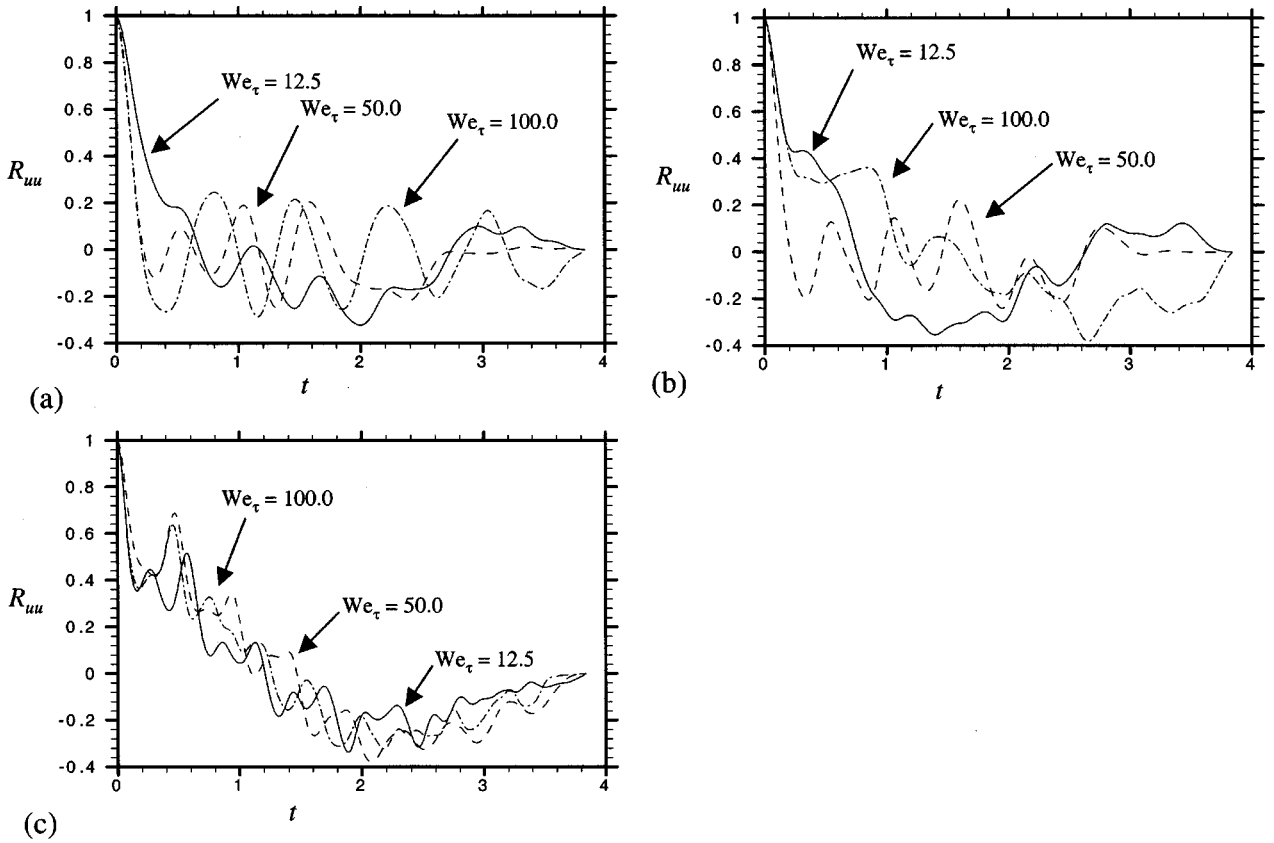

FIG. 1. Autocorrelation function R_{uu} for $b = 900$. (a) $y^+ = 4.0$; (b) $y^+ = 14.6$; (c) $y^+ = 100$.

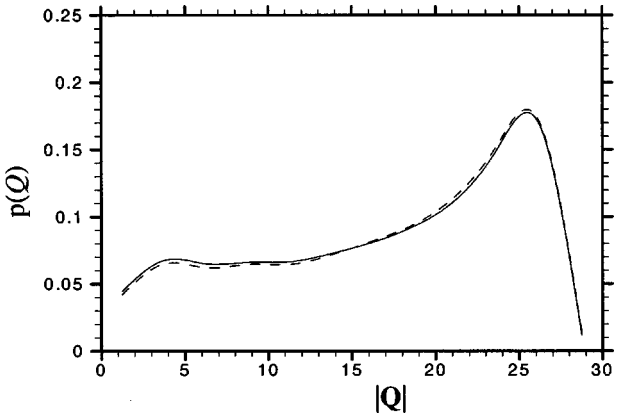

FIG. 2. Probability distribution function for chain extension at $y^+=14.6$ for $We_\tau=100$, $b=900$ for $64\times65\times64$ mesh (solid lines), and $64\times97\times64$ mesh (dashed lines).

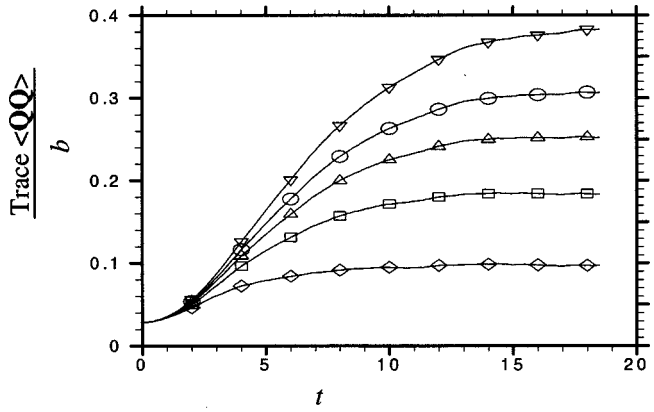

FIG. 4. Variation of averaged trace$\langle\mathbf{QQ}\rangle$ as a function of time for $y^+=14.6$, $b=100$, and $We_\tau=12.5$ ($\diamond$), 25.0 ($\square$), 37.5 ($\triangle$), 50.0 ($\circ$), 75.0 ($\triangledown$).

work were performed with $64(\text{in}\,x)\times65(\text{in}\,y)\times64(\text{in}\,z)$ and $64(\text{in}\,x)\times97(\text{in}\,y)\times64(\text{in}\,z)$ meshes for $Re_\tau=125$ and a $64(\text{in}\,x)\times97(\text{in}\,y)\times64(\text{in}\,z)$ mesh for $Re_\tau=180$. Note that periodicity conditions were applied along the streamwise and spanwise directions, with their respective sizes chosen to adequately capture the streaky structures and the elongated vortical structures, respectively.[46] In the two periodic directions, x, z, Fourier representations were used, whereas, in the nonhomogeneous wall-normal direction a Chebyshev approximation was employed. The (dimensionless) time-step size, Δt, used in the viscoelastic simulations is typically $10^{-4}\,h/u_\tau$ whereas in the Newtonian case it is $10^{-3}\,h/u_\tau$. The friction Reynolds numbers $Re_\tau=125$ and 180 correspond to mean flow Reynolds numbers based on the channel half-width (Re_m) of 1840 and 2800, respectively.

We_τ values used in this study range between 6.25 and 125. For the FENE–P fluid with $L^2=900$ and $\beta=0.9$, $We_\tau=6.25$ roughly corresponds to the onset of DR whereas for $We_\tau=125$ DR of 37% is seen.[68] The percentage DR vs We_τ for $L^2=900$ and $\beta=0.9$ is presented in Table I. Performing BDS of dumbbell trajectories at every spatial location in the mesh and for every time step in DNS is computationally demanding. For this reason, we primarily focus on $y^+=4$ (viscous sublayer), 14.6 (buffer layer), and 100 (turbulent core) for $Re_\tau=125$ and $y^+=6.1$ (viscous sublayer), 21.2 (buffer layer) for $Re_\tau=180$ although results for several other locations are also reported for certain selected cases. The time interval for performing BDS is chosen by examining the autocorrelation functions so that the correlation between the subsequent DNS data sets is $\geqslant$90%. This procedure is illustrated by using an example in Figs. 1(a)–1(c) that show the autocorrelation function R_{uu} for the streamwise velocity component u obtained from the (viscoelastic) DNS at $y^+=4.0$, 14.6, and 100.0, respectively, for $Re_\tau=125$. It is seen that velocity correlations are 90% or more for δt lower than 0.04. Based on this we have chosen time step $\delta t\leqslant0.04$ for the integration of Eq. (8). It should be noted that while integrating Eq. (8) the information from one step is used as initial condition for the next step. Hence we need to ensure a high degree of correlation between the DNS data used for BDS. BDS is performed until a stationary state is obtained at each spatial location. Time averaging is performed over at least 15 eddy turn over times. Typical CPU time for a single run with ensemble size of 2000 is 10 days on a 64 bit DEC-alpha 667 MHz LINUX workstation.

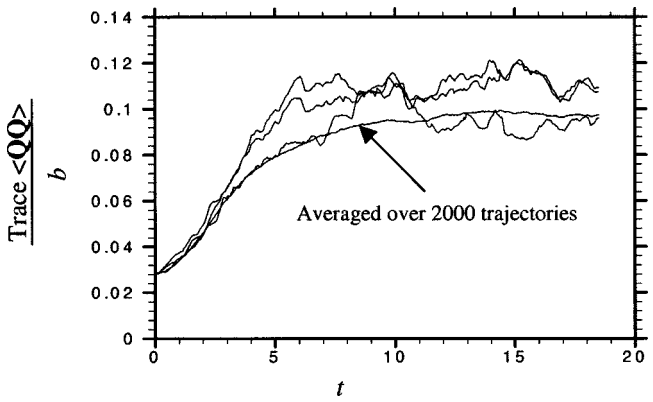

FIG. 3. Variation of trace$\langle\mathbf{QQ}\rangle$ at three different points and averaged trace$\langle\mathbf{QQ}\rangle$ over the entire plane as a function of time for $y^+=14.6$, $b=100$, and $We_\tau=12.5$.

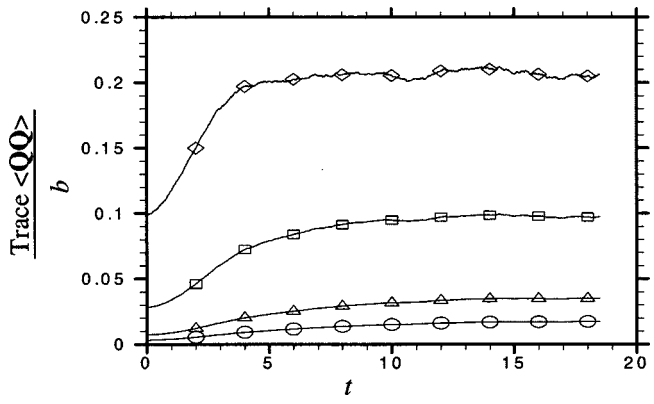

FIG. 5. Variation of averaged trace$\langle\mathbf{QQ}\rangle$ as a function of time for $y^+=14.6$, $We_\tau=12.5$ and $b=25$ ($\diamond$), 100 ($\square$), 400 ($\triangle$), 900 ($\circ$).

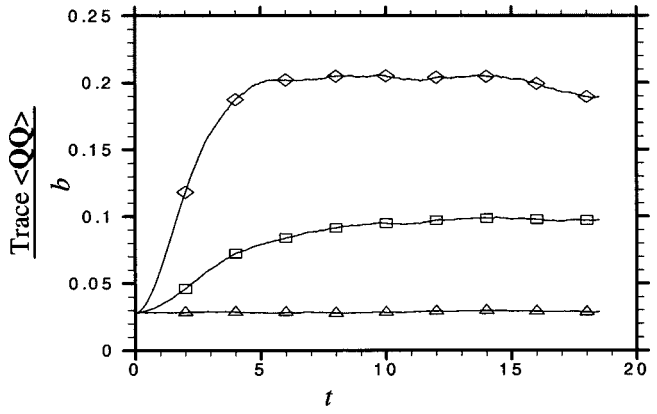

FIG. 6. Variation of averaged trace$\langle \mathbf{QQ} \rangle$ as a function of time for $\mathrm{We}_\tau = 12.5$ and $b = 100$ at three different planes $y^+ = 4.0$ ($\diamond$), 14.6 ($\square$), 100.0 ($\triangle$).

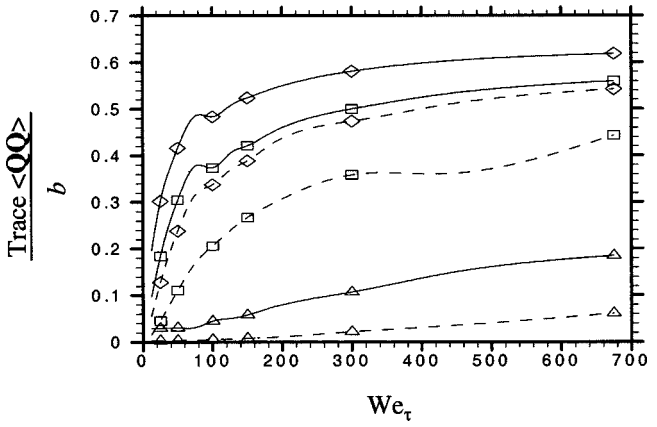

FIG. 7. Variation of averaged trace$\langle \mathbf{QQ} \rangle$ as a function of We_τ for $b = 100$ (solid lines) and for $b = 900$ (dashed lines) at three different planes $y^+ = 4.0$ ($\diamond$), 14.6 ($\square$), 100.0 ($\triangle$).

B. Numerical convergence

We tested the convergence of the BDS results with respect to mesh refinement, ensemble size, and time step for the integration of Eq. (8). Figure 2 shows the normalized probability distribution function for chain extension ($Q \equiv |\mathbf{Q}|$), $p(Q)$, for $\mathrm{We}_\tau = 100$, $\mathrm{Re}_\tau = 125$ obtained by performing BDS for the FENE dumbbell model for $b = 900$ at $y^+ = 14.6$ for two different meshes namely, $64(\mathrm{in}\,x) \times 65(\mathrm{in}\,y) \times 64(\mathrm{in}\,z)$ (solid lines) and $64(\mathrm{in}\,x) \times 97(\mathrm{in}\,y) \times 64(\mathrm{in}\,z)$ (dotted lines). It can be seen from this figure the results obtained with the two different meshes show the same qualitative behavior with a very insignificant quantitative difference. We also note that Sureshkumar *et al.*[46] have shown that for $\mathrm{Re}_\tau = 125$ the mesh used here ($64 \times 65 \times 64$) is sufficient to obtain accurate results for turbulence statistics. Table II shows the influence of ensemble size, N_s, and time step, δt, on the BDS results obtained for the FENE dumbbell model and viscoelastic kinematics for $\mathrm{Re}_\tau = 125$ and $\mathrm{We}_\tau = 125$ in the buffer layer. Once again, it is seen that the BDS results are statistically converged with respect to N_s and δt. Based on these results, ensemble averaging has been performed for 2000 trajectories. We also have verified that the statistical uncertainty associated with these simulations is inversely proportional to the square root of the number of trajectories used as expected.[57]

IV. RESULTS AND DISCUSSION

A. Newtonian kinematics

In this section we present BDS results for the FENE dumbbell model obtained by using Newtonian turbulent channel flow obtained from DNS for $\mathrm{Re}_\tau = 125$. The initial condition for $\mathbf{Q}$ corresponds to equilibrium state of trajectories, i.e., we allow the evolution of $\mathbf{Q}(t)$ in absence of the flow. The evolution of $\mathbf{Q}(t)$ from the initial state subject to Eq. (8) is then computed. Typical result is shown in Fig. 3 where the variation of trace$\langle \mathbf{QQ} \rangle / b$ with time for $y^+ = 14.6$ is presented for $b = 100$, $\mathrm{We}_\tau = 12.5$. It is seen that after an initial transient period trace$\langle \mathbf{QQ} \rangle / b$ becomes statistically stationary and fluctuates around a mean value. As expected at any (x,z) point on the plane $y^+ = 14.6$ trace$\langle \mathbf{QQ} \rangle / b$ fluctuates significantly whereas the ensemble averaged (over the

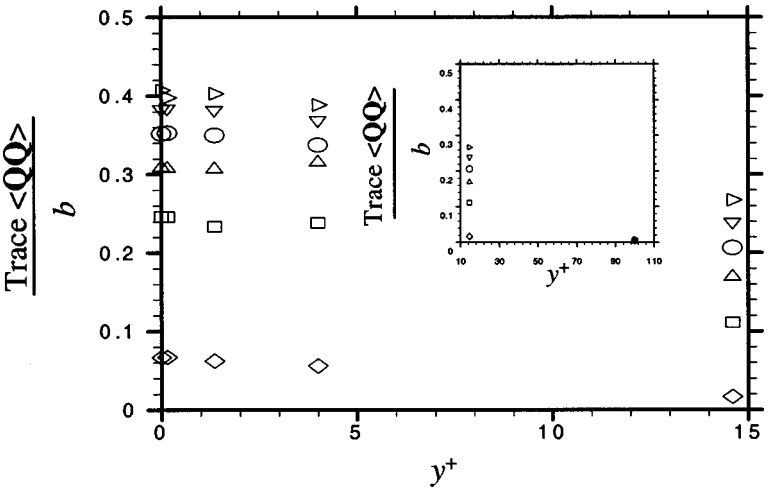

FIG. 8. Variation of averaged trace$\langle \mathbf{QQ} \rangle$ as a function of y^+ for $b = 900$ and $\mathrm{We}_\tau = 12.5$ ($\diamond$), 50.0 ($\square$), 75.0 ($\triangle$), 100.0 ($\bigcirc$), 125.0 ($\triangledown$), 150.0 ($\triangleright$).

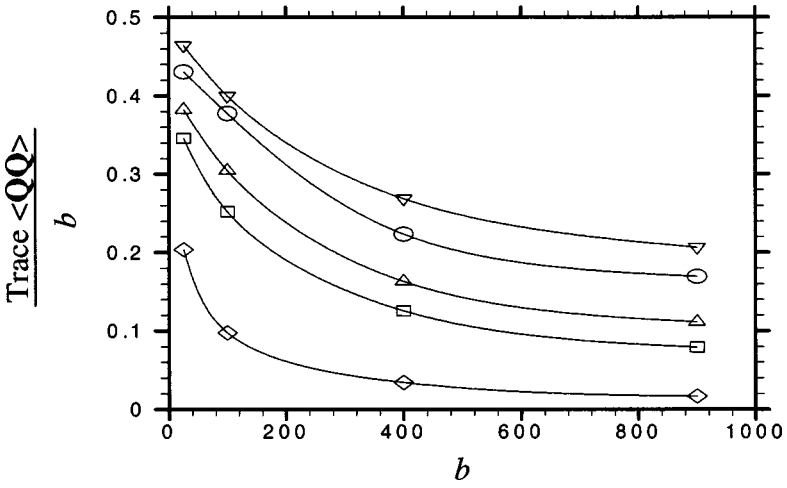

FIG. 9. Variation of trace$\langle \mathbf{QQ} \rangle$ as a function of b for $y^+ = 14.6$ and $\mathrm{We}_\tau = 12.5$ ($\diamond$), 37.5 ($\square$), 50.0 ($\triangle$), 75.0 ($\bigcirc$), 100.0 ($\triangledown$).

entire plane) value has much lower fluctuations. In order to perform time averaging, only the ensembled average data in the statistically stationary regime is used.

Figure 4 shows the variation of trace$\langle \mathbf{QQ} \rangle / b$ with time for $y^+ = 14.6$ for various values of We_τ and $b = 100$. It is seen that as We_τ increases the magnitude of trace$\langle \mathbf{QQ} \rangle / b$ increases. It is also seen that for a lower value of We_τ the stationary state is reached earlier than for a higher value of We_τ. This implies the expected trend that as the polymer relaxation time is increased the polymer chain takes more time to achieve a stationary configuration.

Figure 5 shows the variation of trace$\langle \mathbf{QQ} \rangle / b$ with time at $y^+ = 14.6$ for $\mathrm{We}_\tau = 12.5$ and $b = 25$, 100, 400, 900. It is seen that as b increases the magnitude of trace$\langle \mathbf{QQ} \rangle / b$ decreases. This implies that for a fixed We_τ and Re_τ a polymer chain with a higher maximum extensibility b will produce a lower percentage molecular extension. Figure 6 shows the variation of trace$\langle \mathbf{QQ} \rangle / b$ with time for $b = 100$ and $\mathrm{We}_\tau = 12.5$ at three different planes $y^+ = 4.0$ (within the viscous sublayer), 14.6 (within the buffer layer), and 100.0 (in the turbulent core). It can be seen that molecular extension is the greatest in the viscous sublayer while it is the lowest in the

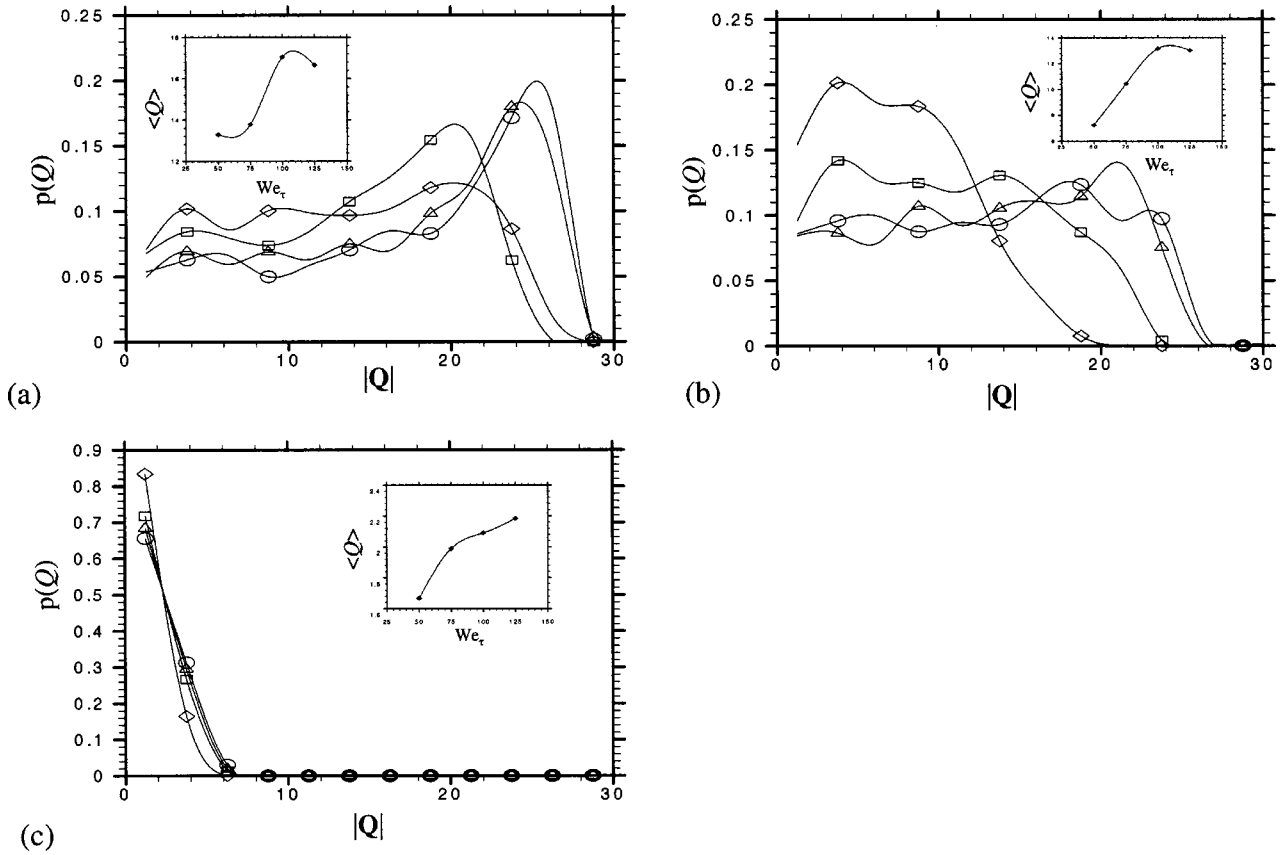

FIG. 10. Probability distribution function for chain extension at $\mathrm{We}_\tau = 50$ ($\diamond$), 75 ($\square$), 100 ($\triangle$), 125 ($\bigcirc$) for $b = 900$. (a) $y^+ = 4.0$; (b) $y^+ = 14.6$; (c) $y^+ = 100$. Inset shows the variation of averaged molecular extension with We_τ.

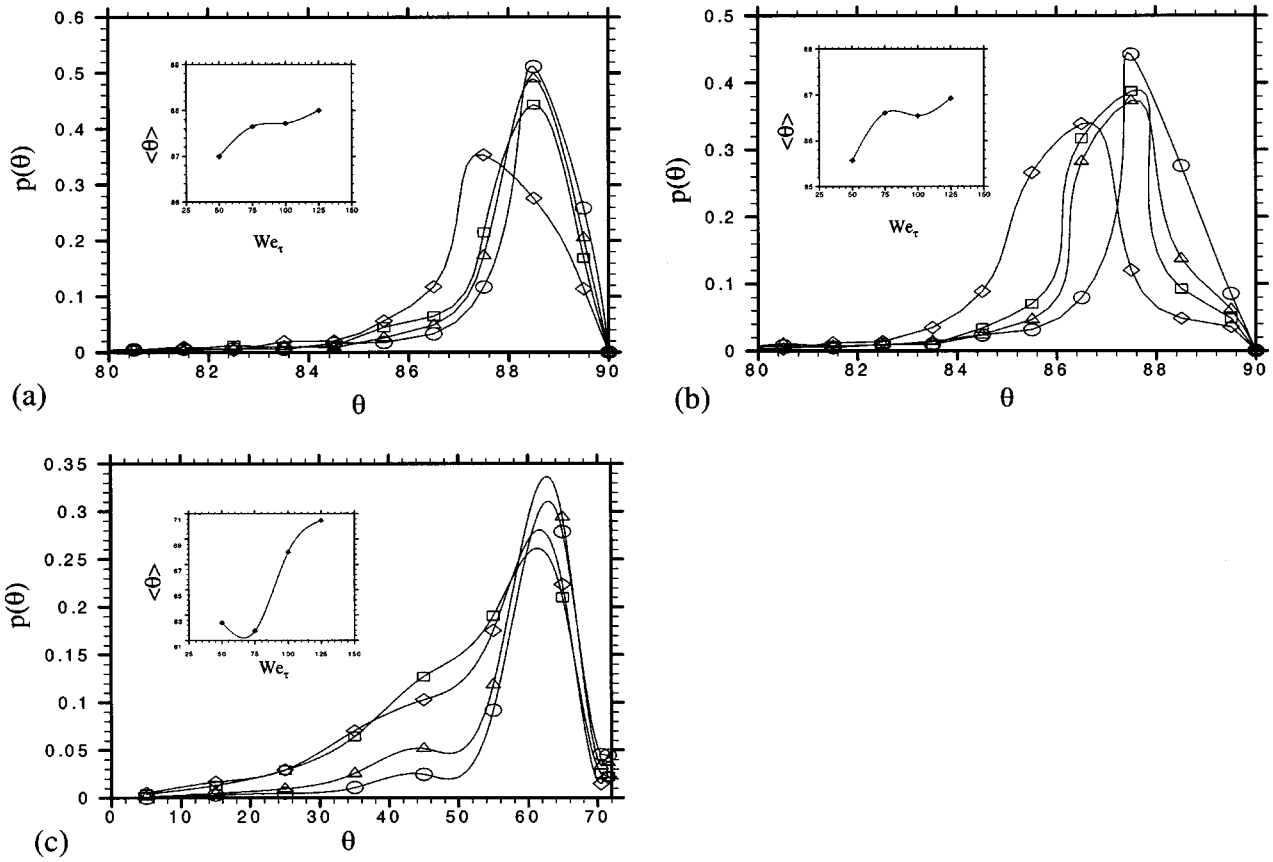

FIG. 11. Orientation distribution at $\mathrm{We}_\tau=50$ ($\diamond$), 75 ($\square$), 100 ($\triangle$), 125 ($\bigcirc$) for $b=900$. (a) $y^+=4.0$; (b) $y^+=14.6$; (c) $y^+=100$. Inset shows the variation of averaged orientation with We_τ.

turbulent core. This implies that a polymer chain experiences greatest configurational changes in the viscous sublayer and lowest in the turbulent core. This is not surprising since a polymer chain will experience greatest configurational changes if it moves from a nearly isotropic flow regime (core) to a highly anisotropic flow one near the wall.

Results similar to those reported in Figs. 4–6 are used to construct Figs. 7–9. Figure 7 shows the variation of $\mathrm{trace}\langle\mathbf{QQ}\rangle/b$ as a function of We_τ at three different planes $y^+=4.0$, 14.6, 100.0 for $b=100$ and $b=900$. It can be seen from this figure that for a given chain extensibility value (i.e., parameter b is kept constant), the chain extension characterized by $\mathrm{trace}\langle\mathbf{QQ}\rangle$ tends to approach an asymptotic value with increasing We_τ. Once again it is clearly seen that as b increases the percentage molecular extension decreases. Figure 8 shows the variation of $\mathrm{trace}\langle\mathbf{QQ}\rangle/b$ as a function of y^+ for $b=900$ and $\mathrm{We}_\tau=12.5$, 50.0, 75.0, 100.0, 125.0, 150.0. It can be seen from this figure that $\mathrm{trace}\langle\mathbf{QQ}\rangle/b$ is maximum near the wall and decreases rapidly to a minimum value at the channel centerline. Figure 9 shows the variation of $\mathrm{trace}\langle\mathbf{QQ}\rangle/b$ with b at $y^+=14.6$ for various Weissenberg number values. It can be seen that a combination of larger values of b and We_τ leads to larger values of chain extension. Moreover, it is shown that the chain extension tends to approach an asymptotic value with increasing b for a given Weissenberg number.

Figure 10(a) shows the normalized probability distribution function (pdf) for chain extension, $p(Q)$, for $\mathrm{We}_\tau=50$, 75, 100, 125 for $b=900$ and $y^+=4.0$. The pdf obtained for $\mathrm{We}_\tau=100$ and 125 are practically identical. These trends are reflected in the values of mean chain extension $\langle Q\rangle$ reported in the inset in Fig. 10(a). It can be seen that as We_τ is increased, $\langle Q\rangle$ increases and tends to asymptote at around $\mathrm{We}_\tau=125$. Similar conclusions can be drawn from Figs. 10(b) and 10(c) where we plot $p(Q)$ for $\mathrm{We}_\tau=50$, 75, 100, 125 for $b=900$ and $y^+=14.6$ and $y^+=100.0$, respectively. Figures 11(a)–11(c) show the pdf for the orientation θ with respect to the gradient direction (y), $p(\theta)$, corresponding to Figs. 10(a)–10(c). It can be seen from Fig. 10(a) that $p(\theta)$ for $\mathrm{We}_\tau=100$ and 125 are practically identical. These trends are also reflected in the values of mean orientation $\langle\theta\rangle$ reported in the inset in Figs. 11(a)–11(c). It is seen that in the viscous sublayer and the buffer layer a polymer chain is more or less aligned to the mean flow direction (x) while in the turbulent core it is not.

B. Viscoelastic kinematics

In this section we present results obtained from BDS for the FENE and FENE–P dumbbell models and viscoelastic kinematics for $\mathrm{Re}_\tau=125$. We first present results for the FENE model. Figure 12(a) shows $p(Q)$ for $\mathrm{We}_\tau=12.5$, 25, 50, 75, 100, 125 for $b=900$ and $y^+=4.0$. It can be seen that for values of $\mathrm{We}_\tau\leqslant 25$, the distribution is skewed to lower values of $|\mathbf{Q}|$. However, as We_τ is increased, $p(Q)$ is strongly skewed to higher values. Moreover, $p(Q)$ obtained

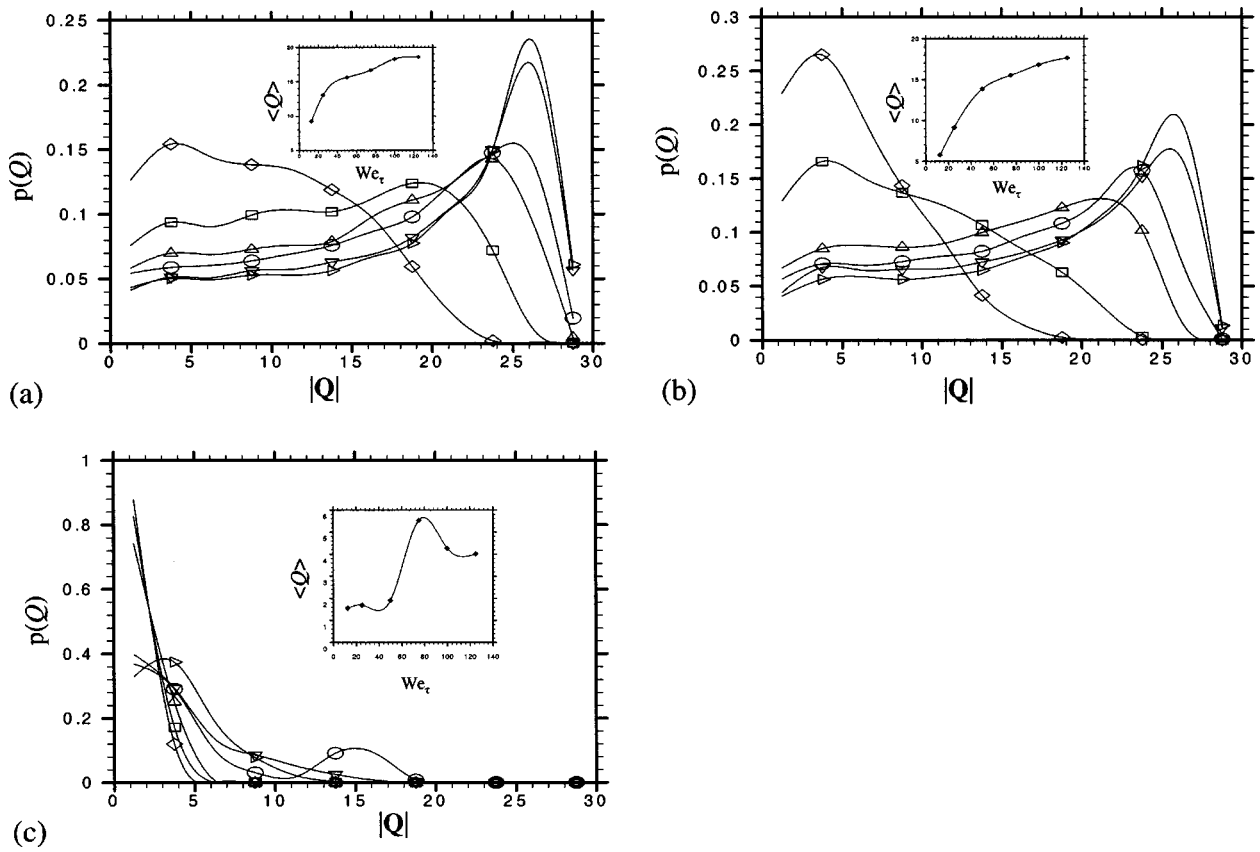

FIG. 12. Probability distribution function for chain extension obtained using the FENE dumbbell model at $We_\tau = 12.5$ ($\diamond$), 25 ($\square$), 50 ($\triangle$), 75 ($\bigcirc$), 100 ($\triangledown$), 125 ($\triangleright$) for $b = 900$. (a) $y^+ = 4.0$; (b) $y^+ = 14.6$; (c) $y^+ = 100$. Inset shows the variation of averaged molecular extension with We_τ.

for $We_\tau = 100$ and 125 are practically identical as reflected in the data for $\langle Q \rangle$ reported in the inset in Fig. 12(a). It is also instructive to examine the contribution to trace$\langle \mathbf{QQ} \rangle$ arising from dumbbells with a given range of mean extension. This statistics can be represented by the percentage contribution function, $\rho(Q)$, defined such that $\rho(Q')dQ'$ represents the percentage contribution to trace$\langle \mathbf{QQ} \rangle$ arising from dumbbells with mean extension between Q' and $Q' + dQ'$. In Fig. 13(a) we plot $\rho(Q)$ corresponding to the $p(Q)$ data presented in Fig. 12(a). It can be seen that as We_τ is increased the contribution from highly extended polymer molecules progressively increases. Inset in Fig. 13(a) shows the variation of percentage contribution to total stress, x_T, arising from trajectories with $Q \geq 0.8\sqrt{b}$ as a function of Weissenberg number. It can be seen from this inset that x_T increases as we increase We_τ and eventually asymptotes. It can be also seen from Fig. 13(a) that $\rho(Q)$ for $We_\tau = 100$ and $We_\tau = 125$ nearly overlap consistent with the asymptotic behavior seen for $\langle |\mathbf{Q}| \rangle$ in Fig. 12(a). This observation is consistent with the asymptotic trend seen in percentage DR for $We_\tau \geq 100$.[68] Moreover for DR $>35\%$ approximately 50% of the total stress is contributed by the small fraction of highly extended molecules. This analysis clearly shows that highly extended molecular states play a very central role in determining the maximum achievable DR for any Re_τ. Hence flow induced scission of the highly extended molecules can greatly deteriorate the drag reducing capability of the additives, as observed experimentally.[69]

Similar conclusions can be observed from Figs. 12(b) and 13(b) where we plot $p(Q)$ and $\rho(Q)$, respectively, for $b = 900$ and $y^+ = 14.6$ which corresponds to a location in the buffer layer. However, in the turbulent core, the behavior is different as shown in Figs. 12(c) and 13(c). It can be seen that $\langle |\mathbf{Q}| \rangle$ remains practically at its equilibrium value ($=\sqrt{3}$) for $We_\tau \leq 40$ and increases sharply to a maximum at $We_\tau \approx 75$ and decreases to a value greater than the equilibrium one for $We_\tau \geq 75$. This indicates that as DR increases the interaction between the polymer and turbulence transcends the buffer region into the turbulent core. However, the chain extension in the core is insignificant as compared to that in the buffer layer. This is also reflected in the data for $\rho(Q)$ reported in Fig. 13(c). Inset in Fig. 13(c) shows that x_T is identically zero. Table III shows a comparison of x_T for vari-

TABLE III. Percentage contribution to the total stress x_T arising from trajectories with $Q \geq 0.8\sqrt{b}$.

	$y^+ = 4.0$	$y^+ = 14.6$	$y^+ = 100.0$
We_τ	x_T	x_T	x_T
12.5	0.0%	0.0%	0.0%
25.0	2.53%	0.01%	0.0%
50.0	18.15%	5.22%	0.0%
75.0	31.34%	16.60%	0.0%
100.0	47.87%	33.66%	0.0%
125.0	50.69%	40.24%	0.0%

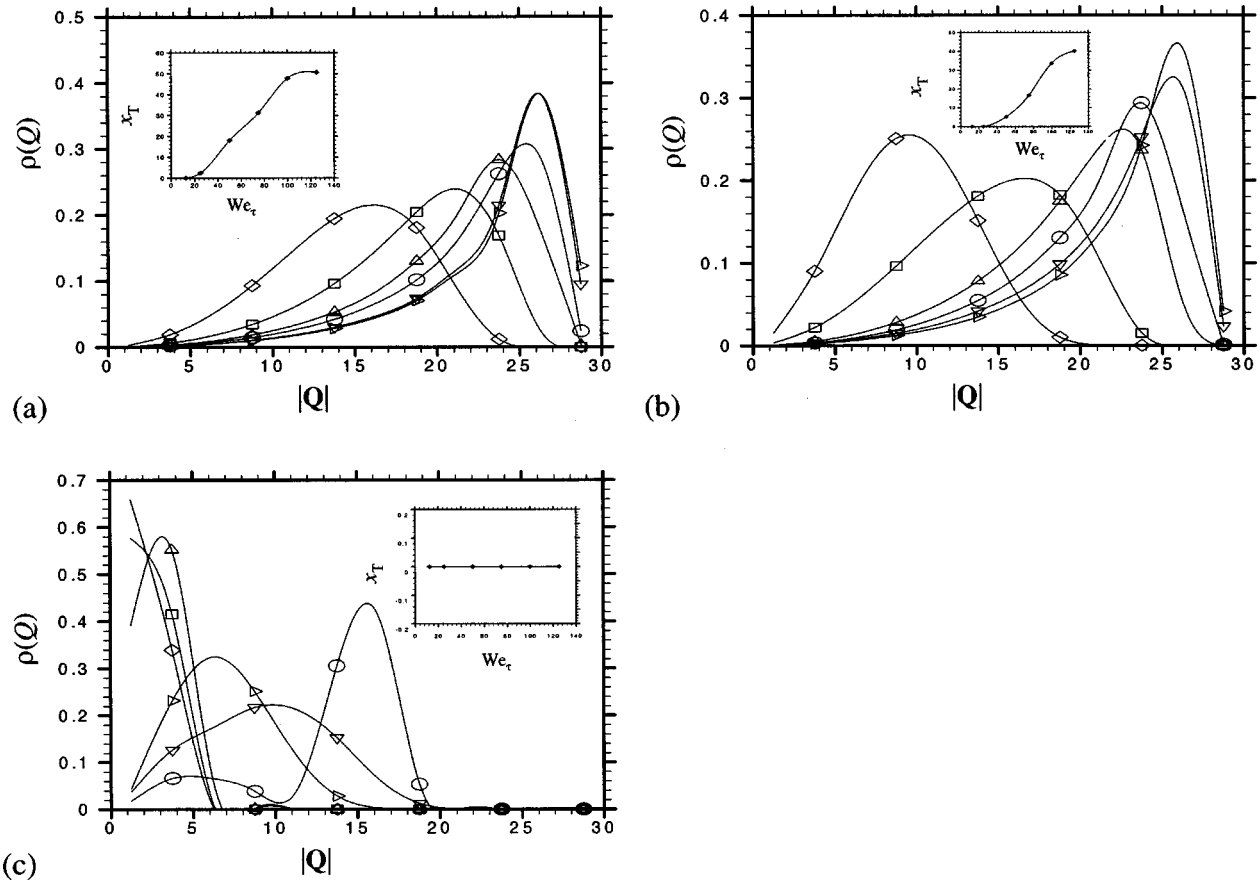

FIG. 13. Variation of % contribution to molecular extension as a function of extension obtained using the FENE dumbbell model at $We_\tau = 12.5$ (◇), 25 (□), 50 (△), 75 (○), 100 (▽), 125 (▷) for $b = 900$. (a) $y^+ = 4.0$; (b) $y^+ = 14.6$; (c) $y^+ = 100$. Inset shows % contribution to the total stress, x_T, arising from the trajectories with $Q \geq 0.8\sqrt{b}$.

ous values of We_τ in the viscous sublayer, buffer layer and the turbulent core. It is seen that for a given Weissenberg number x_T is the largest in the viscous sublayer while it is practically zero in the turbulent core. Figures 14(a)–14(c) show the distribution function $p(\theta)$ for the orientation θ with respect to the gradient direction (y) corresponding to Figs. 12(a)–12(c). It is seen that in the viscous sublayer and the buffer layer the mean orientation is practically independent of Weissenberg number. In the turbulent core ($y^+ = 100.0$) $\langle\theta\rangle$ increases, attains a maxima at around $We_\tau = 90$, and decreases as Weissenberg number is further increased.

Results similar to those reported in Figs. 12–14 are shown in Figs. 15–17 obtained from the BDS using FENE–P dumbbell model and viscoelastic kinematics for $L^2 = 900$. It can be seen that the instantaneous value of Q can exceed the maximum average extensibility L, as was expected. However, the satisfaction of the FENE–P model criterion requires that the ensemble average $\langle \mathbf{Q}^2 \rangle \leq L^2$. Inset in Fig. 16 shows the variation of percentage contribution to total stress, y_T, arising from the "violated states," i.e., configurational states with $Q > L$, as a function of Weissenberg number. It can be seen that y_T increases as we increase We_τ and eventually asymptotes. In the viscous sublayer and the buffer layer this contribution is approximately 70% and 66%, respectively, for $We_\tau = 125$ at which DR of 37% is seen.[68] Table IV shows a comparison of y_T for various values of We_τ in the viscous sublayer, buffer layer, and the turbulent core. It is seen that for a given Weissenberg number y_T is the largest in the viscous sublayer and the lowest in the turbulent core. Since the major contribution to viscoelastic stress arises from the near wall region, this clearly indicates that quantitative predictions of percent DR cannot be made with the FENE–P model where the model parameters are determined based on the molecular details of the additive.

1. Influence of kinematics on mean square extension

Figure 18 shows the influence of flow kinematics on trace of $\langle \mathbf{QQ} \rangle$ for $y^+ = 4.0$, 14.6, 100 and $b = 900$ for various We_τ values for the FENE dumbbell model. It is seen that

TABLE IV. Percentage contribution to the total stress y_T from violated states.

	$y^+ = 4.0$	$y^+ = 14.6$	$y^+ = 100.0$
We_τ	y_T	y_T	y_T
12.5	15.3%	0.85%	0.0%
25.0	43.9%	20.9%	0.0%
50.0	59.3%	49.4%	0.0%
75.0	64.5%	58.4%	33.5%
100.0	69.5%	61.9%	35.2%
125.0	70.4%	65.9%	39.1%

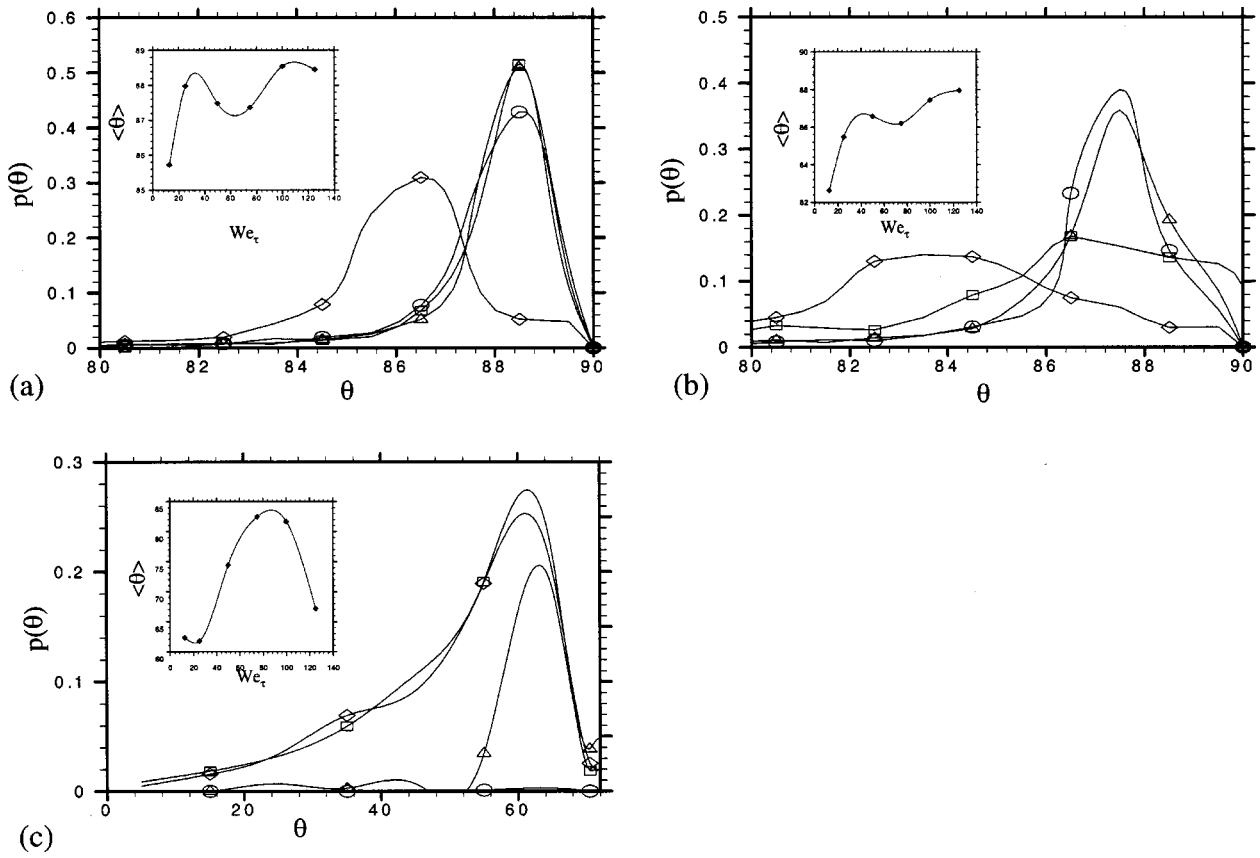

FIG. 14. Orientation distribution obtained using the FENE dumbbell model at $We_\tau = 12.5$ (◇), 25 (□), 50 (△), 75 (○) for $b = 900$. (a) $y^+ = 4.0$; (b) $y^+ = 14.6$; (c) $y^+ = 100$. Inset shows the variation of averaged orientation with We_τ.

viscoelastic kinematics produce larger mean square extension as compared to the Newtonian one. It is also seen from this figure that for a given value of b the mean square extension in the buffer layer increases as We_τ is increased and eventually asymptotes at $We_\tau = 125$. This is in agreement with the fact that for a given value of b as We_τ increases the %DR increases and eventually asymptotes at $We_\tau = 125$.[68] Moreover, the mean square extension at given We_τ is slightly larger in the viscous sublayer ($y^+ = 4.0$) than in the buffer layer ($y^+ = 14.6$). In addition, the mean square extension produced in the *core* by Newtonian kinematics is very insignificant in comparison to that produced by viscoelastic kinematics. This is due to the fact that polymer chain extension in the buffer layer is much more significant in the viscoelastic flows. Hence, during ejection/sweep cycles much more highly extended chains are introduced into the core. It can also be seen that in the turbulent core, mean square extension increases as we increase Weissenberg number, attains a maximum for $We_\tau \approx 75$, and decreases for $We_\tau > 75$. As pointed out earlier this behavior is qualitatively different from those seen in the viscous sublayer and the buffer layer. The maximum extension seen in the core could correspond to a ''locking in'' mechanism where the time scale of bursting T is comparable to the average fluid relaxation time λ. In other words, $\lambda/T \approx 1$ for $We_\tau \approx 75$ for which maximum extension is seen in the core. However it is also possible that this is an artifact of performing decoupled BDS. In either case as seen from Table V, the magnitude of the chain extension in the core is negligible compared to that in the

TABLE V. Comparison of percentage mean square extension (relative to b) from Newtonian and viscoelastic kinematics (New: Newtonian; vis: viscoelastic).

	$y^+ = 4.0$		$y^+ = 14.6$		$y^+ = 100.0$	
We_τ	New	vis	New	vis	New	vis
12.5	5.6%	12.9%	1.7%	4.9%	0.34%	0.36%
25.0	12.8%	23.8%	4.6%	12.3%	0.35%	0.41%
50.0	23.8%	33.1%	11.1%	26.8%	0.38%	0.55%
75.0	31.5%	37.6%	16.9%	33.0%	0.50%	6.34%
100.0	33.8%	44.1%	20.6%	37.9%	0.56%	3.30%
125.0	36.9%	45.3%	23.9%	41.3%	0.67%	2.45%

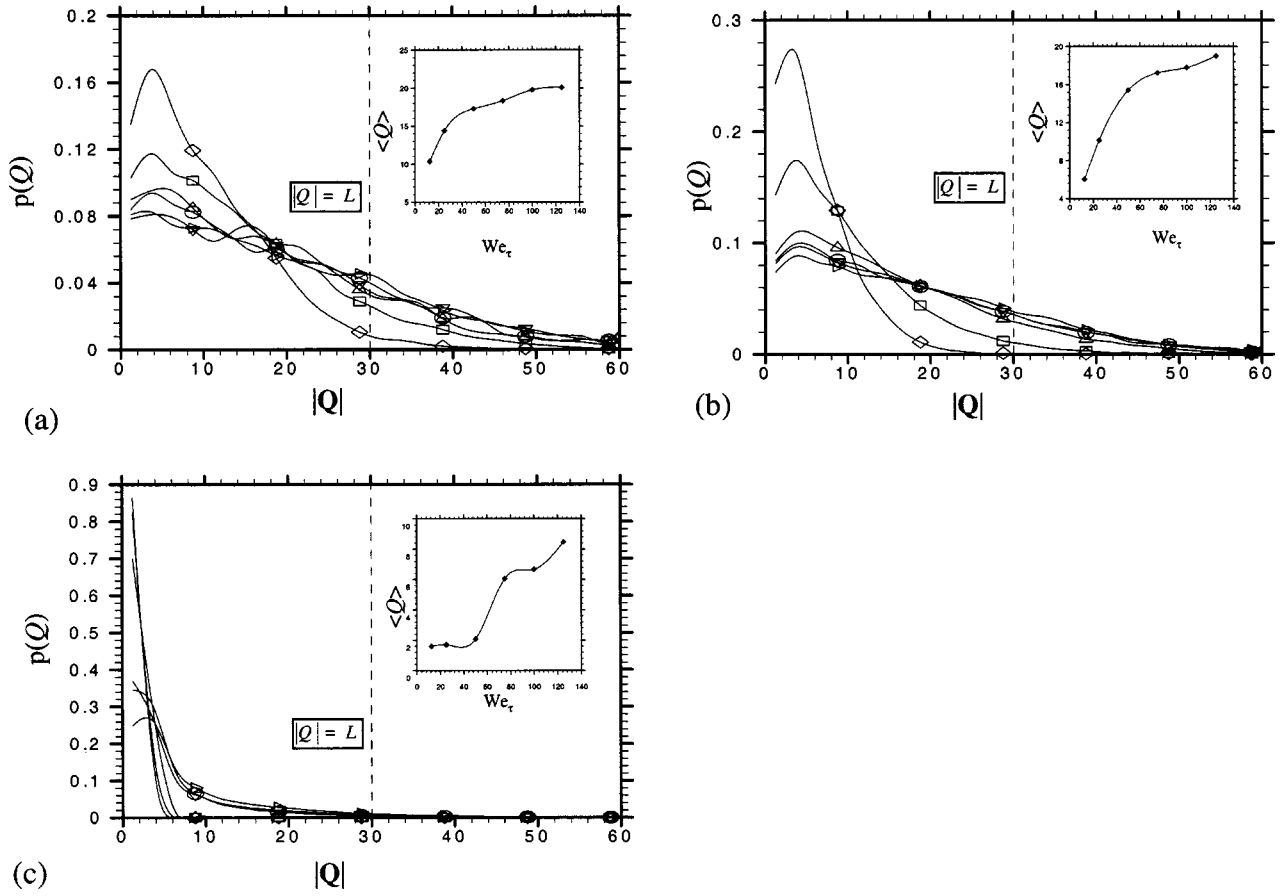

FIG. 15. Probability distribution function for chain extension obtained using the FENE–P dumbbell model at $We_\tau = 12.5$ (◇), 25 (□), 50 (△), 75 (○), 100 (▽), 125 (▷) for $L^2 = 900$. (a) $y^+ = 4.0$; (b) $y^+ = 14.6$; (c) $y^+ = 100$. Inset shows the variation of averaged molecular extension with We_τ.

buffer layer. Consequently the maximum in extension seen in the core is unlikely to have an appreciable effect on DR.

2. Influence of turbulent fluctuations on mean square extension

In order to investigate the influence of turbulent fluctuations on the mean square extension we compared trace$\langle \mathbf{QQ} \rangle$ obtained from the BD–DNS to the mean square extension obtained from BDS using the mean turbulent flow velocity profile $U(y)$. Figures 19(a)–19(c) show the variation of the difference (normalized with b) in the mean square extension obtained from the simulation and that obtained for the mean shear flow as a function of Weissenberg number at three different locations: $y^+ = 4.0$, 14.6, 100.0 for three different values of b. It is apparent from these figures that this normalized difference is practically nonexistent in the viscous sublayer while it is highest in the turbulent core. Further, it is seen that in the buffer layer the enhanced extension caused by turbulent fluctuations attains two maxima, one located at $We_\tau \approx 30$ while the other located at $We_\tau \approx 100$, which are practically independent of b. However, in the turbulent core we observe only one such maximum which is located at $We_\tau \approx 75$. In the buffer layer, the first maximum could be attributed to the fact that the initial increase in u_{rms} is rapid with increasing Weissenberg number and then the rate of increase is slowed down.[68] Meanwhile, v_{rms} and w_{rms} de-

TABLE VI. Influence of maximum extensibility on percentage mean square extension (relative to b).

	$y^+ = 4.0$					
We_τ	FENE $b=900$	FENE $b=1600$	FENE $b=3600$	FENE–P $L^2=100$	FENE–P $L^2=400$	FENE–P $L^2=900$
12.5	12.9%	9.4%	5.6%	46.5%	28.2%	19.1%
25.0	23.8%	19.3%	13.8%	63.2%	47.6%	36.6%
50.0	33.1%	28.9%	22.6%	74.0%	61.6%	52.1%
75.0	37.6%	33.7%	27.4%	78.8%	68.1%	58.7%
100.0	44.1%	41.0%	35.4%	83.9%	75.8%	67.4%
125.0	45.3%	41.5%	36.2%	84.8%	77.2%	69.9%

TABLE VII. Influence of maximum extensibility on percentage mean square extension (relative to b).

	$y^+ = 14.6$					
We_τ	FENE $b=900$	FENE $b=1600$	FENE $b=3600$	FENE–P $L^2=100$	FENE–P $L^2=400$	FENE–P $L^2=900$
12.5	4.9%	3.1%	1.6%	26.0%	11.3%	6.8%
25.0	12.3%	9.2%	5.7%	43.7%	26.6%	19.1%
50.0	26.8%	22.8%	17.1%	66.6%	51.7%	41.6%
75.0	33.0%	29.1%	23.5%	70.9%	60.9%	51.6%
100.0	37.9%	35.2%	30.9%	76.4%	64.3%	55.2%
125.0	41.3%	38.0%	31.9%	80.4%	70.4%	61.1%

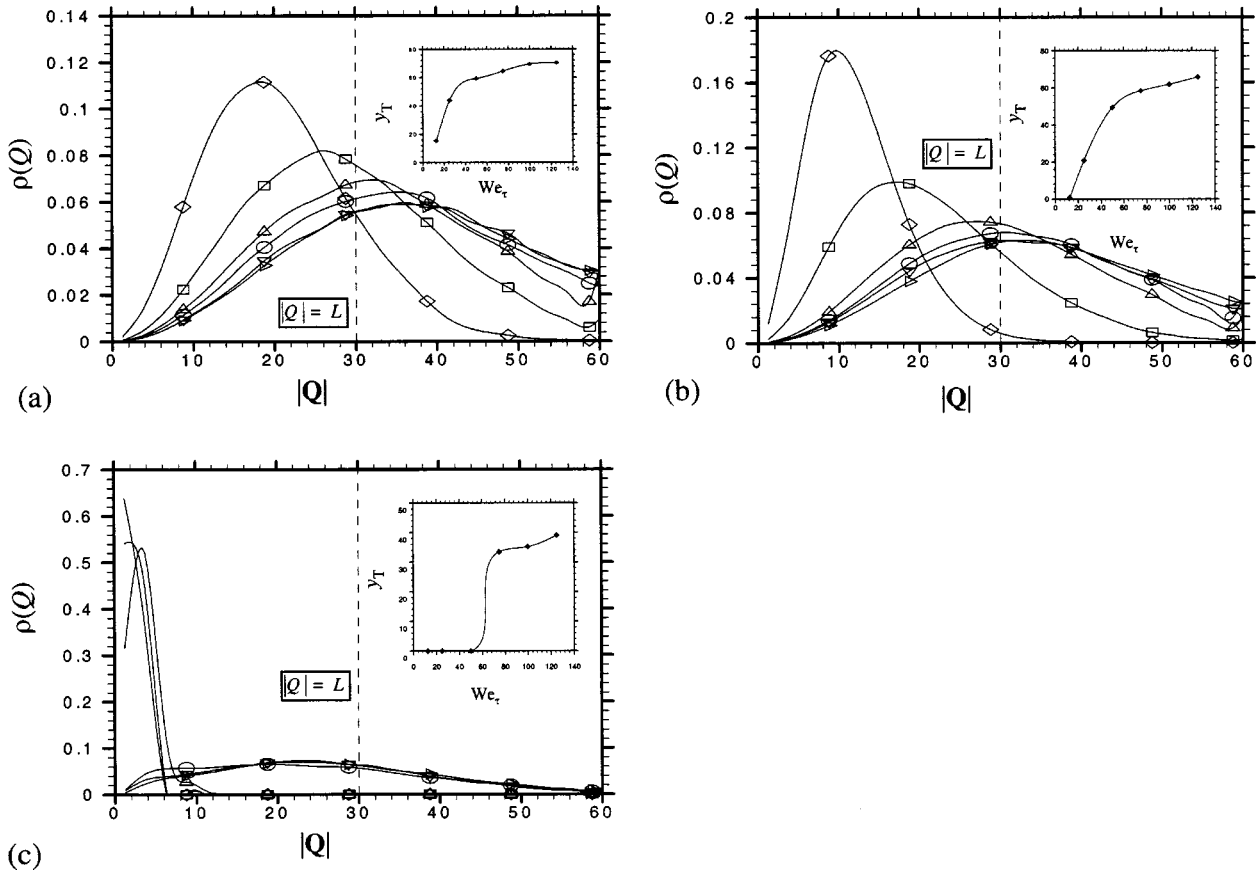

FIG. 16. Variation of % contribution to molecular extension as a function of extension obtained using the FENE–P dumbbell model at $We_\tau = 12.5$ (◇), 25 (□), 50 (△), 75 (○), 100 (▽), 125 (▷) for $L^2 = 900$. (a) $y^+ = 4.0$; (b) $y^+ = 14.6$; (c) $y^+ = 100$. Inset shows % contribution to the total stress, y_T, arising from the violated states.

crease with increasing Weissenberg number. This mechanism is not applicable to the turbulent core since the fluctuations are more or less isotropic. The maximum seen in the normalized difference in the turbulent core may be attributed to global events, i.e., sweep-ejection cycles that could have time scales comparable to the relaxation time of the molecule.

3. Influence of extensibility parameter on mean square extension: Comparison of FENE and FENE–P predictions

Figures 20(a) and 20(b) show the influence of maximum extensibility parameter b on the ftrace$\langle \mathbf{QQ} \rangle / b$ for various Weissenberg number values in the viscous sublayer ($y^+ = 4.0$) and the buffer layer ($y^+ = 14.6$), respectively. Also presented in the same figures are the results obtained for trace$\langle \mathbf{QQ} \rangle / b$ for the mean (shear) flow. It can be seen that stochastic nature of the turbulent flow produces more chain extension. It is also seen that a combination of larger values of b and We_τ leads to a larger value of chain extension though percentage chain extension decreases. Moreover, it can be seen that the chain extension tends to approach an asymptotic value with increasing We_τ for a given b. Tables VI and VII show comparison of trace$\langle \mathbf{QQ} \rangle / b$ achieved for various values of b (for FENE) and L^2 (for FENE–P) in the viscous sublayer and the buffer layer, respectively. As we increase b or L^2 at given We_τ trace$\langle \mathbf{QQ} \rangle / b$ achieved decreases although the mean square extension increases. This is clearly demonstrated in Figs. 21(a) and 21(b) where we plot trace$\langle \mathbf{QQ} \rangle / b$ achieved in the buffer layer as a function of b or L^2 for FENE and FENE–P dumbbell models, respectively. Comparison of Figs. 21(a) and 21(b) shows qualitatively similar behavior for trace$\langle \mathbf{QQ} \rangle$ vs b or L^2. This, and the data reported in Tables VI and VII, suggest that the predictions of the two models for trace$\langle \mathbf{QQ} \rangle$ may be matched by suitable renormalization of the maximum extensibility parameter. Furthermore one can see from Figs. 20(a) and 20(b) that trace$\langle \mathbf{QQ} \rangle$ obtained from FENE dumbbell model simulation for $b = 1600$ is approximately the same as that obtained from

TABLE VIII. Influence of maximum extensibility on percentage mean square extension (relative to b).

	$y^+ = 100.0$					
We_τ	FENE $b = 900$	FENE $b = 1600$	FENE $b = 3600$	FENE–P $L^2 = 100$	FENE–P $L^2 = 400$	FENE–P $L^2 = 900$
12.5	0.36%	0.20%	0.09%	3.22%	0.83%	0.37%
25.0	0.41%	0.23%	0.10%	3.61%	0.94%	0.43%
50.0	0.55%	0.31%	0.14%	5.11%	1.43%	0.69%
75.0	6.34%	5.9%	5.48%	18.11%	11.41%	10.04%
100.0	3.30%	2.14%	1.21%	21.13%	13.96%	12.51%
125.0	2.45%	1.47%	0.68%	25.28%	18.47%	17.64%

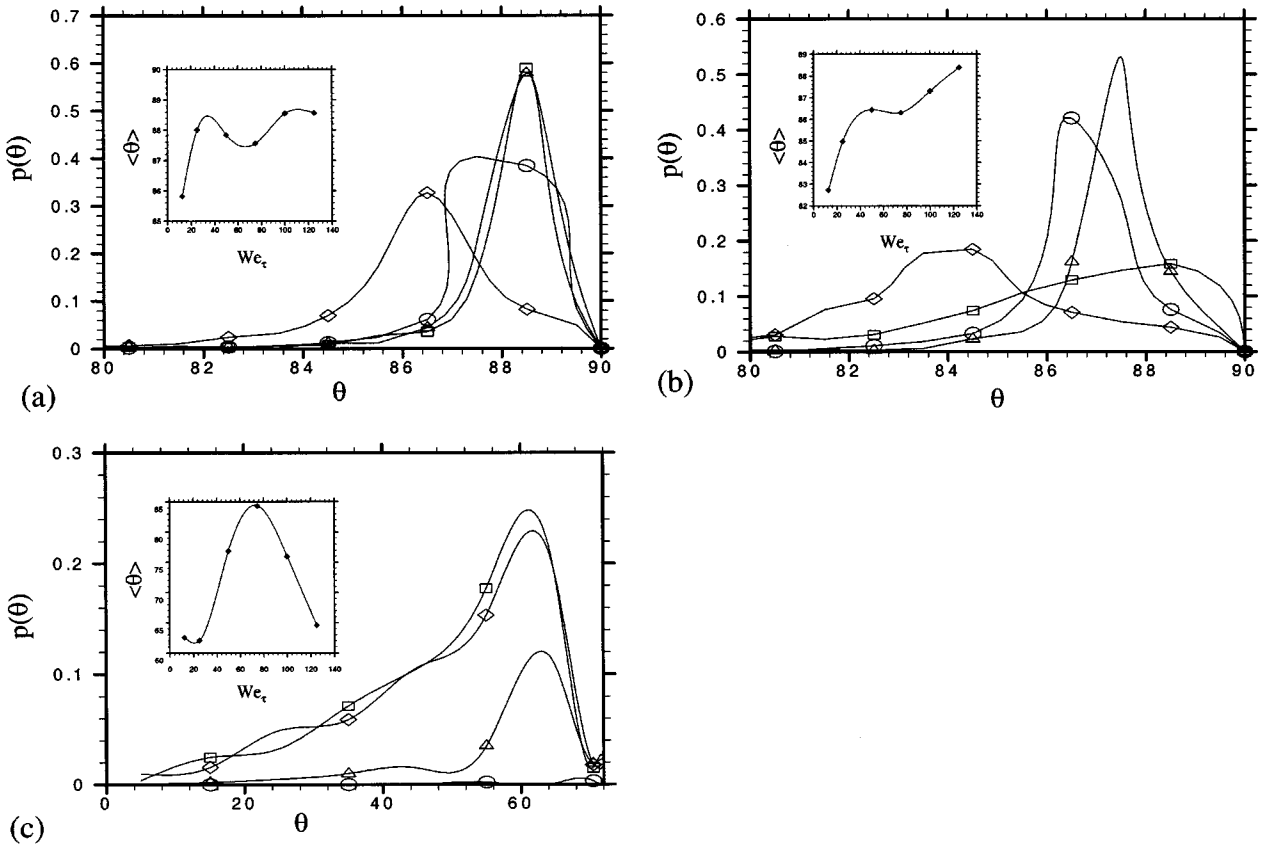

FIG. 17. Orientation distribution obtained using the FENE–P dumbbell model at $We_\tau = 12.5$ (◇), 25 (□), 50 (△), 75 (○) for $L^2 = 900$. (a) $y^+ = 4.0$; (b) $y^+ = 14.6$; (c) $y^+ = 100$. Inset shows the variation of averaged orientation with We_τ.

FENE–P dumbbell model simulation for $L^2 = 900$ for given We_τ. We investigated whether similar behavior could be seen for other values of b as well. Figures 22(a) and 22(b) show the variation of the trace$\langle \mathbf{QQ} \rangle / b$ with We_τ in the viscous sublayer ($y^+ = 4.0$) and the buffer layer ($y^+ = 14.6$), respectively, for three different values of $b = 169, 676, 1521$. The values for maximum chain extensibility for the FENE–P model that match the FENE model predictions are found to be $L^2 = 100$, 400, and 900, respectively. The insets in Figs. 22(a) and 22(b) show the variation of b/L^2 as a function of L^2. It can be seen that a ratio of $b/L^2 = 1.7$ is required in order to obtain quantitative agreement between the predictions of the FENE and FENE–P dumbbell models. A similar conclusion is reached from Figs. 23(a) and 23(b) where we show variation of $\langle \mathbf{QQ} \rangle_{xy} / b$ with We_τ corresponding to Figs. 22(a) and 22(b). If we were to match plateau extensional viscosity predicted by FENE and FENE–P dumbbell models a ratio of $b/L^2 = 1$ is needed. On the other hand, a ratio of $b/L^2 = 7/3$ is required to match the zero shear viscosity. Since in a wall-bounded turbulent flow shear and

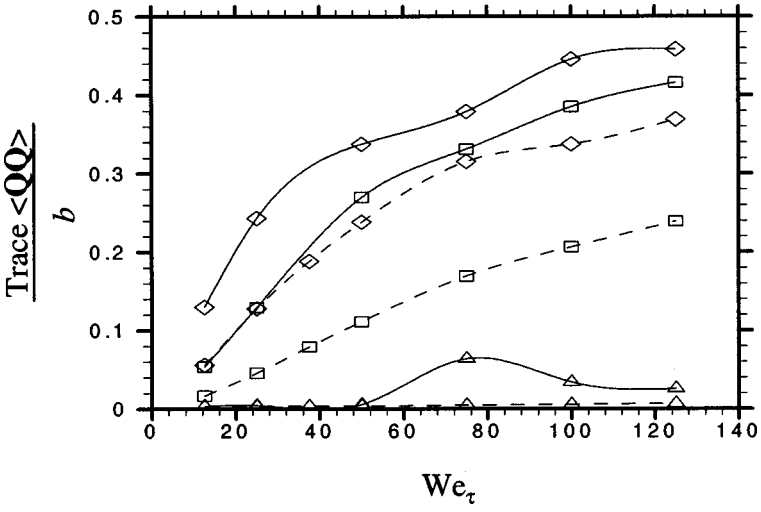

FIG. 18. Variation of trace$\langle \mathbf{QQ} \rangle$ as a function of We_τ obtained using the FENE dumbbell model for $b = 900$ for viscoelastic kinematics (solid lines) and Newtonian kinematics (dashed lines) at $y^+ = 4.0$ (◇), 14.6 (□), 100.0 (△).

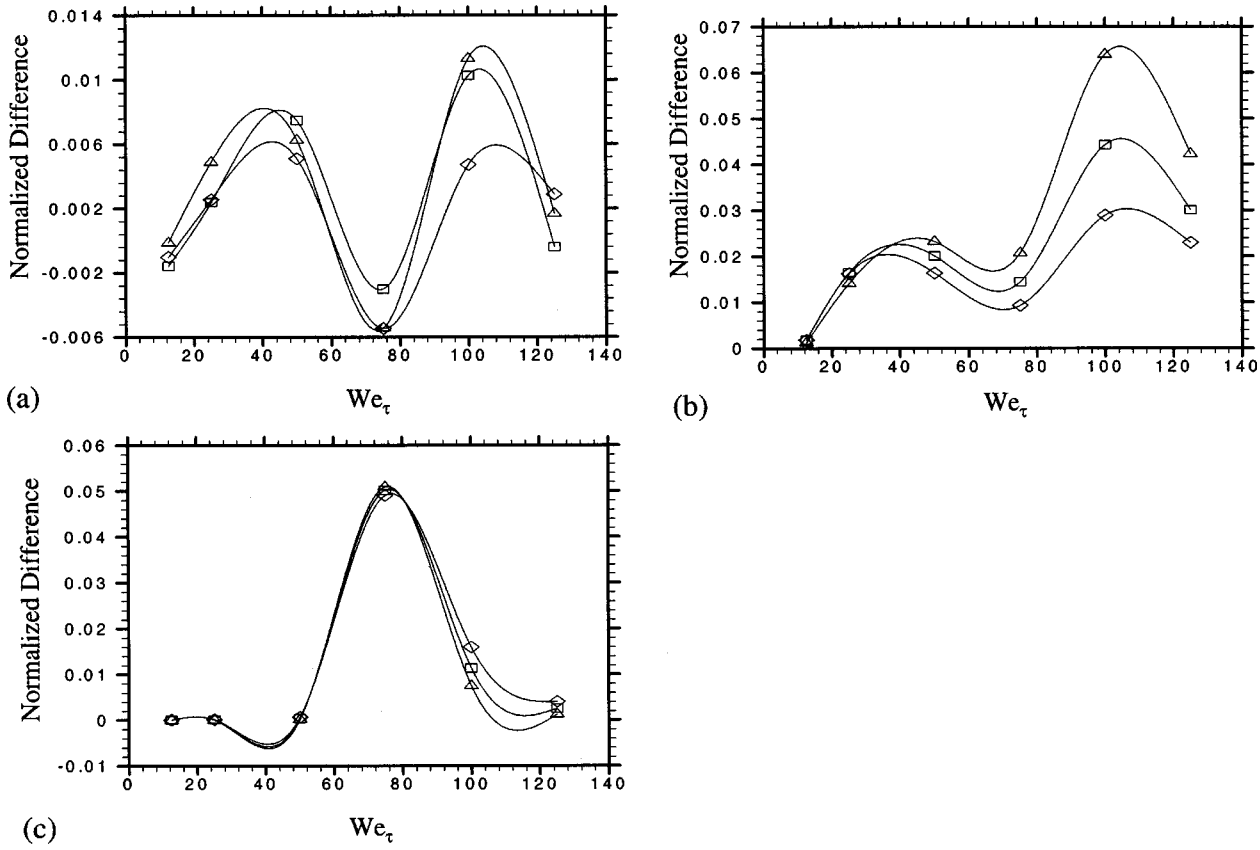

FIG. 19. Variation of normalized difference in molecular extension with Weissenberg number obtained using the FENE dumbbell model for $b=900$ ($\diamond$), 1600 ($\square$), 3600 ($\triangle$). (a) $y^+=4.0$; (b) $y^+=14.6$; (c) $y^+=100$.

elongational deformations are present, it is not surprising that the b/L^2 ratio required to obtain agreement between the predictions of the FENE and FENE–P dumbbell models would lie somewhere in between these two limits. However, as mentioned earlier a chain never reaches its maximum extension in the flows under consideration. Hence, a better estimate of the lower bound for this ratio could be obtained based on the transient extensional viscosity. Hence, we have also examined the influence of the renormalization of the extensibility parameter on the prediction of transient extensional viscosity in purely extensional flow given by $v_x=\dot{\epsilon}x$; $v_y=-\frac{1}{2}\dot{\epsilon}y$; $v_z=-\frac{1}{2}\dot{\epsilon}z$. The results are shown in Figs. 24(a) and 24(b) where $\eta_E\equiv(\tau_{xx}-\tau_{zz})/\dot{\epsilon}$ is plotted as a function of the extensional strain ($\dot{\epsilon}t$) for $\lambda\dot{\epsilon}=3$ and 15, respectively. For large values of strain the plateau extensional viscosity value $\eta_{E\infty}$ is reached. As expected $\eta_{E\infty}$ is linearly proportional to b or L^2. However, for relatively small strains ($2\leqslant\dot{\epsilon}t\leqslant5$) the FENE and FENE–P responses are significantly different, i.e., FENE predicts a gradual increase in η_E while FENE–P predicts a sudden transition to the $\eta_{E\infty}$ limit. Note that these range of strains ($2\leqslant\dot{\epsilon}t\leqslant5$) in an extensional flow would produce chain extension values similar to those

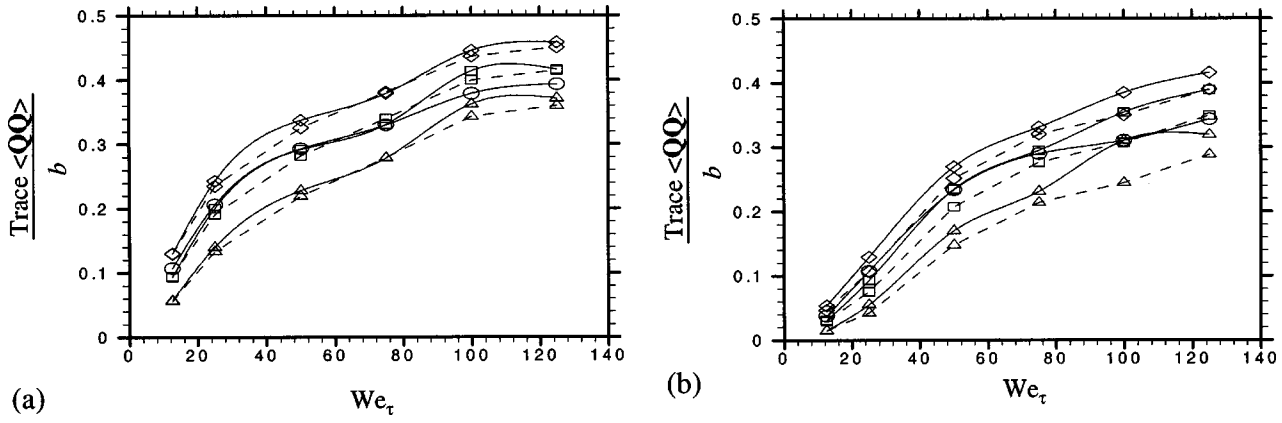

FIG. 20. Mean square extension for FENE: $b=900$ ($\diamond$), 1600 ($\square$), 3600 ($\triangle$) and FENE–P: $L^2=900$ ($\bigcirc$). (a) $y^+=4.0$; (b) $y^+=14.6$. Dashed lines correspond to the results obtained from BDS in the absence of turbulent fluctuations.

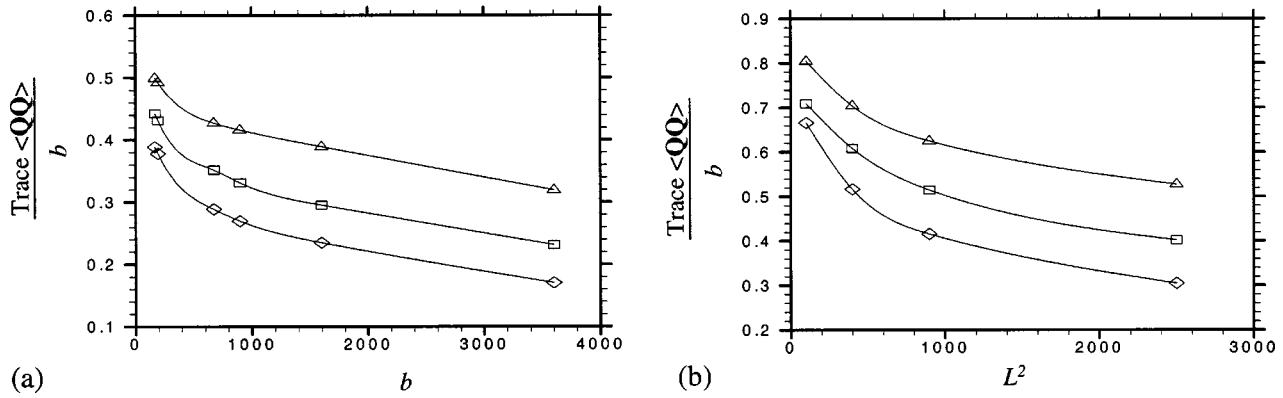

FIG. 21. Mean square extension as a function of extensibility parameter for $We_\tau = 50$ ($\diamond$), 75 ($\square$), 125 ($\triangle$) at $y^+ = 14.6$. (a) FENE; (b) FENE–P.

predicted in the viscous sublayer and the buffer layer in the turbulent flow. As seen from Figs. 24(a) and 24(b) the disparity between the FENE and FENE–P predictions for small strain values in pure extensional flows can also be reduced by applying the renormalization discussed above. This clearly shows that although the renormalization brings the predictions of the two models closer it does not provide a one to one correspondence between the transient extensional viscosity of the two models. This is expected as the flow kinematics are nonhomogeneous and contain both shear and extensional gradients in velocity.

4. Mean square extension in the turbulent core

It was shown in Fig. 18 that for $b = 900$ the dependance of chain extension with We_τ is qualitatively different in the turbulent core as compared to that in the buffer layer. We investigated whether similar behavior could be seen for other values of b as well. Figure 25 shows the variation of mean square extension with Weissenberg number in the turbulent core ($y^+ = 100$) obtained from FENE dumbbell model simulation for three different values of $b = 900$, 1600, and 3600 and that obtained from FENE–P dumbbell model simulation for $L^2 = 900$. The behavior of the trace$\langle \mathbf{QQ} \rangle / b$ vs We_τ data obtained from FENE dumbbell model simulation is similar for all three values of b, i.e., mean square extension increases as we increase Weissenberg number, attains a maximum for $We_\tau \approx 75$ and decreases for $We_\tau > 75$. However, FENE–P dumbbell model predicts mean square extension which progressively increases as we increase Weissenberg number. Table VIII shows comparison of percentage chain extension achieved for various values of b in the turbulent core.

C. Influence of flow inertia

In this section we investigate the influence of Reynolds number on polymer chain dynamics by performing BDS in conjunction with DNS for $Re_\tau = 180$. In particular, we would like to investigate the influence of Reynolds number on the pdfs for stretch and orientation and the renormalization discussed in Sec. IV B 3. We perform BDS of FENE and FENE–P dumbbells for $25 \leqslant We_\tau \leqslant 100$ at $y^+ = 6.1$ (viscous sublayer) and 21.2 (buffer layer) for $Re_\tau = 180$.

Figure 26(a) shows $p(Q)$ for $We_\tau = 25$, 50, 75, 100 for $b = 900$ in the buffer layer. It can be seen that as We_τ is increased, $p(Q)$ gets progressively skewed to higher values of Q. Moreover, the dependence of the pdf on We_τ is similar to that seen for $Re_\tau = 125$. A comparison shows that pdf for $Re_\tau = 180$ has more extended states. However, the fraction of states with low to moderate extension is lower. The inset in Fig. 26(a) shows the variation of mean chain extension $\langle Q \rangle$ as a function of We_τ. Consequently for a given We_τ the mean chain extension for $Re_\tau = 180$ is only marginally higher

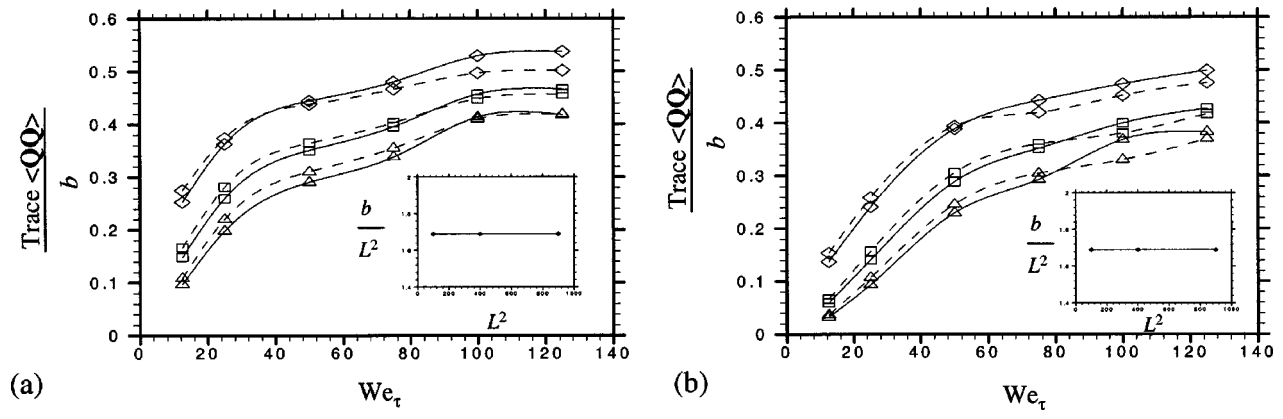

FIG. 22. Mean square extension for FENE (solid lines): $b = 169$ ($\diamond$), 676 ($\square$), 1521 ($\triangle$) and FENE–P (dashed lines): $L^2 = 100$ ($\diamond$), 400 ($\square$), 900 ($\triangle$). (a) $y^+ = 4.0$; (b) $y^+ = 14.6$.

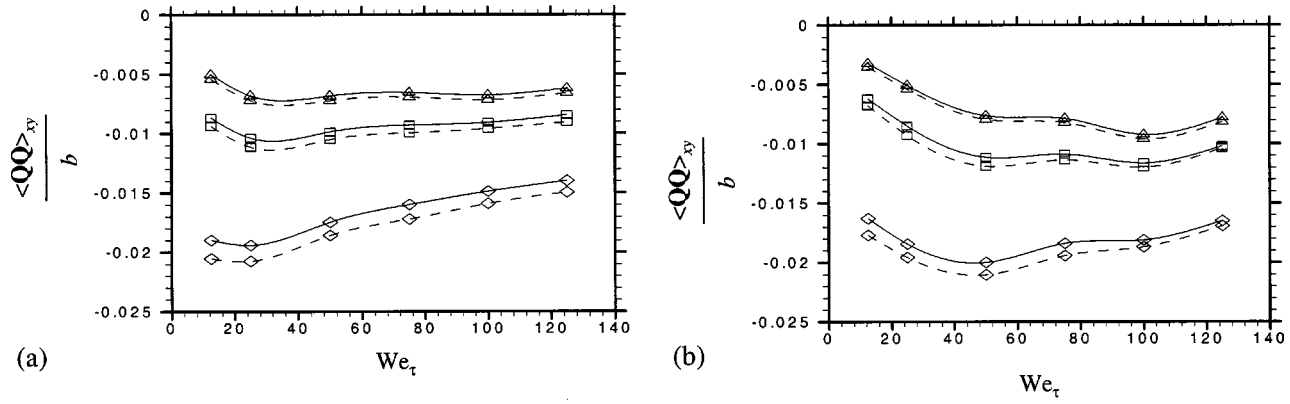

FIG. 23. $\langle \mathbf{QQ} \rangle_{xy}$ for FENE (solid lines): $b=169$ (◇), 676 (□), 1521 (△) and FENE–P (dashed lines): $L^2=100$ (◇), 400 (□), 900 (△). (a) $y^+=4.0$; (b) $y^+=14.6$.

than that for $Re_\tau=125$. This could help explain the relative insensivity of %DR to Re_τ observed in continuum-level simulations and the fact that very high Re_τ and We_τ are required to perform simulations near MDR.[68]

Figures 26(b) shows the pdf for orientation $p(\theta)$ corresponding to Fig. 26(a). It is clear from Figs. 26(a) and 26(b) that increasing Re_τ from 125 to 180 has only minor quantitative influence on the predictions. In both cases, the average orientation approaches 90° indicating flow alignment of the polymers. Results similar to those reported in Figs. 22 and 23 for $Re_\tau=125$ are shown in Figs. 27 and 28 obtained for $Re_\tau=180$. Once again, for a ratio of $b/L^2=1.7$, a fairly good quantitative agreement between the predictions of the FENE and FENE–P dumbbell models is obtained.

V. CONCLUSIONS

Polymer chain dynamics in Newtonian and viscoelastic turbulent channel flows have been simulated by using Brownian dynamics techniques utilizing the FENE and FENE–P dumbbell models. The influence of polymer relaxation time, chain extensibility, and wall shear rate on mean chain extension, pdf of chain stretch and viscoelastic stress has been examined in detail in the viscous sublayer, buffer layer, and turbulent core. Molecular extension is the greatest in the viscous sublayer while it is lowest in the turbulent core. However, the chain extension contributed by turbulent fluctuations is largest in the buffer layer. For a given chain extensibility, the chain extension tends to approach an asymptotic value with increasing Weissenberg number and vice versa. For given values of the Weissenberg and Reynolds numbers the percentage maximum extension achieved decreases although the mean square extension increases. Moreover, the chain extension in viscoelastic (drag-reduced) turbulent channel flow is greater than that in the Newtonian one.

The pdf of Q predicted by the FENE and FENE–P models gets progressively skewed to larger values of Q as DR increases. Moreover, consistent with the observation that $\langle \mathbf{QQ} \rangle$ approaches an asymptotic value with increasing DR, the pdf of Q also becomes relatively insensitive to DR for %DR$\geqslant$30%. Even for DR of 37% the pdf exhibits a long tail of relatively unextended molecules.

It is shown that "violated states" in the FENE–P simulations contribute to a large fraction of the stress. Our findings suggest that the interaction between transient quasi-streamwise vortices and the polymer chain is a key

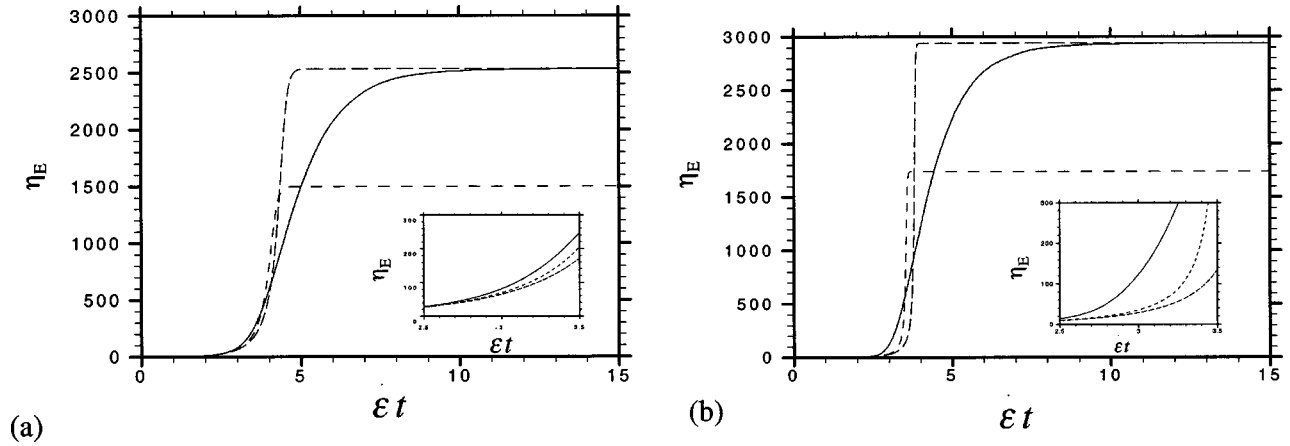

FIG. 24. Variation of η_E with $\dot{\epsilon}t$ for FENE: $b=1521$ (solid lines) and FENE–P: $L^2=900$ (dashed lines), 1521 (long dashed lines). (a) $\lambda\dot{\epsilon}=3$; (b) $\lambda\dot{\epsilon}=15$.

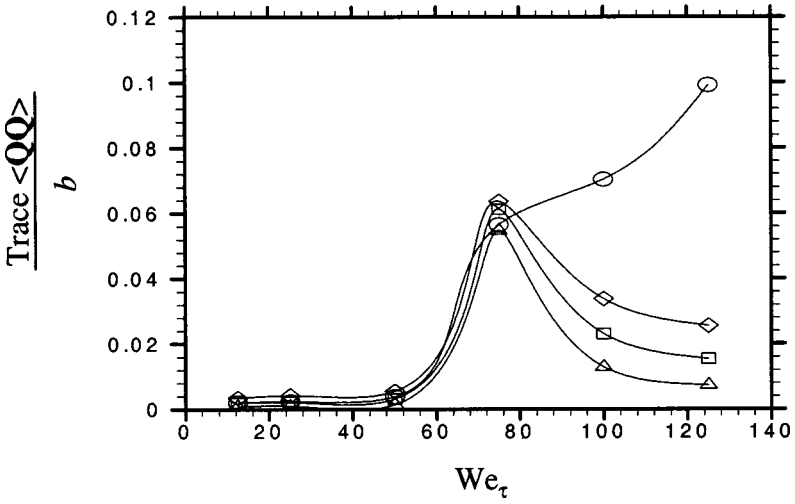

FIG. 25. Mean square extension for FENE: $b=900$ ($\diamond$), 1600 ($\square$), 3600 ($\triangle$) and FENE–P: $L^2=900$ ($\bigcirc$) at $y^+=100.0$.

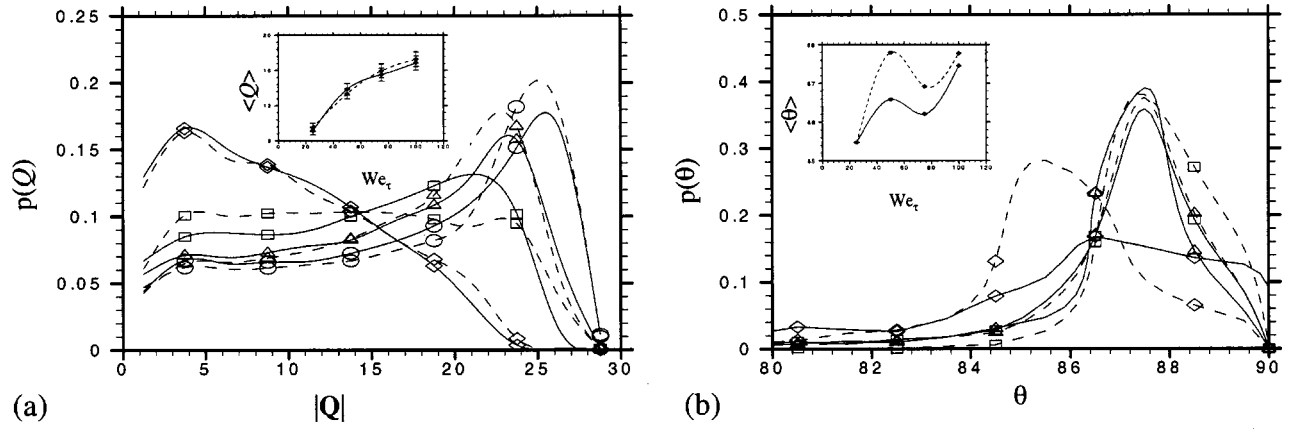

FIG. 26. Probability distribution function for chain extension (a) and orientation distribution (b) in the buffer layer obtained using the FENE dumbbell model for $We_\tau=25$ ($\diamond$), 50 ($\square$), 75 ($\triangle$), 100 ($\bigcirc$) for $b=900$ and $Re_\tau=125$ (solid lines), 180 (dashed lines). Inset shows the variation of averaged molecular extension with We_τ.

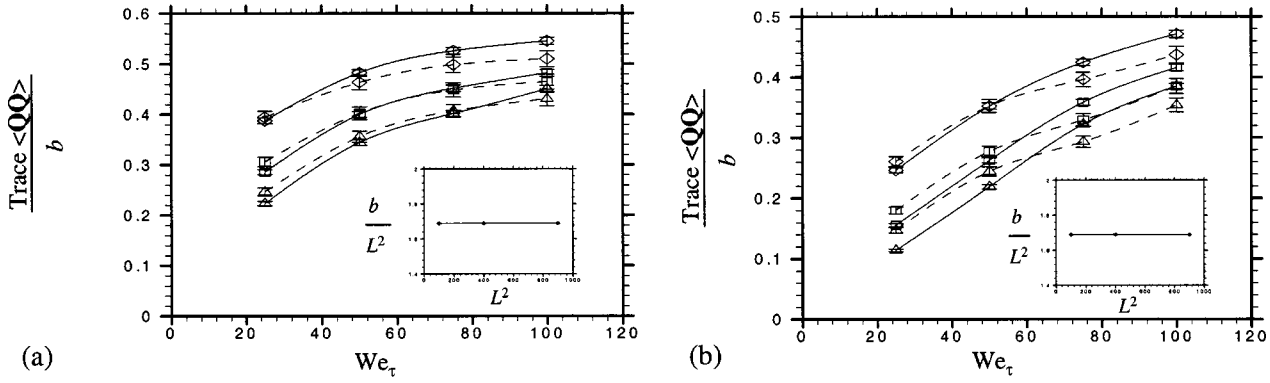

FIG. 27. Mean square extension for FENE (solid lines): $b=169$ ($\diamond$), 676 ($\square$), 1521 ($\triangle$) and FENE–P (dashed lines): $L^2=100$ ($\diamond$), 400 ($\square$), 900 ($\triangle$). (a) $y^+=6.13$; (b) $y^+=21.25$.

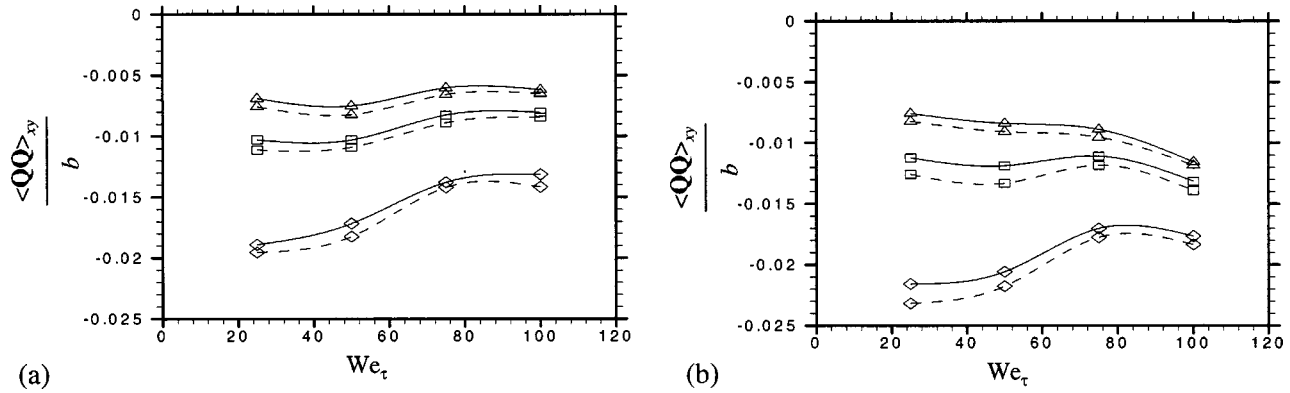

FIG. 28. $\langle \mathbf{QQ} \rangle_{xy}$ for FENE (solid lines): $b=169$ ($\diamond$), 676 ($\square$), 1521 ($\triangle$) and FENE–P (dashed lines): $L^2=100$ ($\diamond$), 400 ($\square$), 900 ($\triangle$). (a) $y^+=6.13$; (b) $y^+=21.25$.

mechanism of chain extension. In other words, the polymer chains on the surface of these vortices undergo large extension whereas the molecular extension is much smaller in the vortex core. This conclusion is supported by self-consistent DNS data[46–50] and models of DR based on the interaction of polymers with exact coherent states.[51,52] The pdf of Q is qualitatively unaffected by the wall shear rate as evidenced by the comparison of BDS results obtained for $\mathrm{Re}_\tau=125$ and 180. As the wall shear rate is increased the fraction of highly extended chains increases. This is accompanied by a reduction in the fraction of chains with low to moderate extension. Hence, $\langle \mathbf{QQ} \rangle$ is only marginally influenced by increasing Re_τ. This could explain the insensitivity of %DR to Re_τ predicted by self-consistent DNS as well as the very high Re_τ and We_τ required in the continuum based DNS to achieve MDR.[68]

Despite the differences in the details of the pdf for Q, the quantitative differences between the predictions of the FENE and FENE–P models for $\langle \mathbf{QQ} \rangle$ in the viscous sublayer and the buffer layer could be practically eliminated by suitable renormalization of the maximum extensibility parameter. This renormalization also reduces the disparity between the FENE and FENE–P model predictions for the shear stress and transient extensional viscosity.

ACKNOWLEDGMENTS

The authors would like to acknowledge the financial support provided by DARPA, Grant No. MDA972-01-1-0007. Partial support from NSF Grant No. CTS-9874813 and the Donors of The Petroleum Research Fund, administered by the ACS through Grant Nos. 38511-AC9 and 37905-AC7, are also acknowledged.

[1] J. Azaiez and G. M. Homsy, "Linear stability of free shear flow of viscoelastic liquids," J. Fluid Mech. **268**, 37 (1994).
[2] J. Azaiez and G. M. Homsy, "Numerical simulation of non-Newtonian free shear flows at high Reynolds numbers," J. Non-Newtonian Fluid Mech. **52**, 333 (1994).
[3] J. M. Rallison and E. J. Hinch, "Instability of a high speed submerged elastic jet," J. Fluid Mech. **288**, 311 (1995).
[4] S. Kumar and G. M. Homsy, "Direct numerical simulation of hydrodynamic instabilities in two and three-dimensional viscoelastic free shear layers," J. Non-Newtonian Fluid Mech. **83**, 249 (1999).
[5] R. Sureshkumar, "Local linear stability characteristics of viscoelastic periodic channel flow," J. Non-Newtonian Fluid Mech. **97**, 125 (2001).
[6] B. Sadanandan and R. Sureshkumar, "Viscoelastic effects on the stability of wall-bounded shear flows," Phys. Fluids **14**, 41 (2002).
[7] R. Sureshkumar and A. N. Beris, "Linear stability analysis of the viscoelastic Poiseuille flow using an Arnoldi orthogonalization algorithm," J. Non-Newtonian Fluid Mech. **56**, 151 (1995).
[8] M. Avgousti and A. N. Beris, "Viscoelastic Taylor–Couette flow: Bifurcation analysis in the presence of symmetries," Proc. R. Soc. London, Ser. A **443**, 17 (1993).
[9] J. L. Lumley, "Drag reduction by additives," Annu. Rev. Fluid Mech. **1**, 367 (1969).
[10] J. L. Lumley, "Drag reduction in turbulent flow by polymer additives," J. Polym. Sci., Part D: Macromol. Rev. **7**, 263 (1973).
[11] J. L. Lumley, "Drag reduction in two phase and polymer flows," Phys. Fluids **20**, S64 (1977).
[12] A. Gyr and H.-W. Bewersdorff, *Drag Reduction of Turbulent Flows by Additives* (Kluwer Academic, Netherlands, 1995).
[13] R. C. Vaseleski and A. B. Metzner, "Drag reduction in the turbulent flow of fiber suspensions," AIChE J. **20**, 301 (1974).
[14] N. S. Berman, "Drag reduction by polymers," Annu. Rev. Fluid Mech. **10**, 47 (1978).
[15] D. K. Oldaker and W. G. Tiederman, "Spatial structure of the viscous sublayer in drag-reducing channel flows," Phys. Fluids **20**, S133 (1977).
[16] W. G. Tiederman, T. S. Luchik, and D. G. Bogard, "Wall-layer structure and drag reduction," J. Fluid Mech. **156**, 419 (1985).
[17] R. F. Blackwelder and R. E. Kaplan, "On the wall structure of the turbulent boundary layer," J. Fluid Mech. **76**, 89 (1976).
[18] T. S. Luchik and W. G. Tiederman, "Turbulent structure in low-concentration drag-reducing channel flows," J. Fluid Mech. **190**, 241 (1988).
[19] D. T. Walker and W. G. Tiederman, "Turbulent structure in a channel flow with polymer injection at the wall," J. Fluid Mech. **218**, 377 (1990).
[20] A. Gyr and H.-W. Bewersdorff, "Change of structures close to the wall of a turbulent flow in a drag reducing fluids," *Structure of Turbulence and Drag Reduction* (Springer, New York, 1989), pp. 215–222.
[21] W. G. Tiederman, "The effect of dilute polymer solution on viscous drag and turbulence structure," *Structure of Turbulence and Drag Reduction* (Springer, New York, 1989), pp. 187–200.
[22] K. J. Harder and W. G. Tiederman, "Drag reduction and turbulent structure in two-dimensional channel flows," Proc. R. Soc. London, Ser. A **336**, 19 (1991).
[23] T. Wei and W. W. Willmarth, "Modifying turbulent structure with drag-reducing polymer additives in turbulent channel flows," J. Fluid Mech. **245**, 619 (1992).
[24] G. Fortuna and T. J. Hanratty, "The influence of drag-reducing polymers on turbulence in the viscous sublayer," J. Fluid Mech. **53**, 575 (1972).
[25] E. R. Corino and R. S. Brodkey, "A visual investigation of the wall region in turbulent flow," J. Fluid Mech. **37**, 1 (1969).
[26] G. L. Donohue, W. G. Tiederman, and M. M. Reischman, "Flow visualization of the near-wall region in a drag-reducing channel flow," J. Fluid Mech. **56**, 559 (1972).
[27] M. M. Reischman and W. G. Tiederman, "Laser-Doppler anemometer

measurements in drag-reducing channel flows,'' J. Fluid Mech. **70**, 369 (1975).
[28]W. D. McComb and L. H. Rabie, ''Laser-Doppler measurements of turbulent structure,'' AIChE J. **28**, 558 (1982).
[29]H. Usui, M. Kodama, and Y. Sano, ''Laser-Doppler measurements of turbulence structure in a drag-reducing pipe flow with polymer injection,'' J. Chem. Eng. Jpn. **21**, 134 (1988).
[30]A. B. Metzner and M. G. Park, ''Turbulent flow characteristics of viscoelastic fluids,'' J. Fluid Mech. **20**, 291 (1964).
[31]F. A. Seyer and A. B. Metzner, ''Turbulence phenomena in drag-reducing systems,'' AIChE J. **15**, 426 (1969).
[32]A. B. Metzner, ''Polymer solution and fiber suspension rheology and their relationship to turbulent drag reduction,'' Phys. Fluids **20**, S145 (1977).
[33]H. W. Bewersdorff and N. S. Berman, ''The influence of flow-induced non-Newtonian fluid properties on turbulent drag reduction,'' Rheol. Acta **27**, 130 (1988).
[34]J. M. J. Den Toonder, F. T. M. Nieuwstadt, and G. D. C. Kuiken, ''The role of elongational viscosity in the mechanism of drag reduction by polymer additives,'' Appl. Sci. Res. **54**, 95 (1995).
[35]H. C. Hershey and J. L. Zakin, ''A molecular approach to predicting the onset of turbulent drag reduction in the turbulent flow of dilute polymer solutions,'' Chem. Eng. Sci. **22**, 1847 (1967).
[36]R. B. Bird, C. F. Curtiss, R. C. Armstrong, and O. Hassager, *Dynamics of Polymeric Fluids* (Wiley, New York, 1987), Vol. 1.
[37]A. N. Beris and B. J. Edwards, *Thermodynamics of Flowing Systems with Internal Microstructure* (Oxford University Press, New York, 1994).
[38]M. J. Rudd, ''Velocity measurements made with a laser Doppler meter on the turbulent pipe flow of a dilute polymer solution,'' J. Fluid Mech. **51**, 673 (1972).
[39]N. S. Berman, ''Flow time scales and drag reduction,'' Phys. Fluids **20**, S168 (1977).
[40]P. G. de Gennes, ''Towards a scaling theory of drag reduction,'' Physica A **140**, 9 (1986).
[41]D. D. Joseph, *Fluid Dynamics of Viscoelastic Liquids* (Springer, New York, 1990).
[42]K. R. Sreenivasan and C. M. White, ''The onset of drag reduction by dilute polymer additives, and the maximum drag reduction asymptote,'' J. Fluid Mech. **409**, 149 (2000).
[43]P. Orlandi, ''A tentative approach to the direct simulation of drag reduction by polymers,'' J. Non-Newtonian Fluid Mech. **60**, 277 (1995).
[44]A. Baron and S. Sibilla, ''DNS of the turbulent channel flow of a dilute polymer solution,'' Appl. Sci. Res. **59**, 331 (1998).
[45]A. N. Beris and R. Sureshkumar, ''Simulation of time-dependent viscoelastic channel Poiseuille flow at high Reynolds numbers,'' Chem. Eng. Sci. **51**, 1451 (1996).
[46]R. Sureshkumar, A. N. Beris, and R. A. Handler, ''Direct numerical simulation of the turbulent channel flow of a polymer solution,'' Phys. Fluids **9**, 743 (1997).
[47]C. D. Dimitropoulos, R. Sureshkumar, and A. N. Beris, ''Direct numerical simulation of viscoelastic turbulent channel flow exhibiting drag reduction: Effect of the variation of rheological parameters,'' J. Non-Newtonian Fluid Mech. **79**, 433 (1998).
[48]C. D. Dimitropoulos, R. Sureshkumar, A. N. Beris, and R. A. Handler, ''Budgets of Reynolds stress, kinetic energy and streamwise enstrophy in viscoelastic turbulent channel flow,'' Phys. Fluids **13**, 1016 (2001).
[49]R. Sureshkumar and A. N. Beris, ''Effect of artificial stress diffusivity on the stability of numerical calculations and the flow dynamics of time-dependent viscoelastic flows,'' J. Non-Newtonian Fluid Mech. **60**, 53 (1995).
[50]Y. Dubief, C. M. White, E. S. G. Shaqfeh, S. K. Lele, and P. Moin, ''On polymer action and coherent structures in viscoelastic flows for low and high drag reduction regimes,'' Phys. Fluids (submitted).
[51]P. A. Stone and M. D. Graham, ''Polymer dynamics in a model of the turbulent buffer layer,'' Phys. Fluids **15**, 1247 (2003).
[52]P. A. Stone, F. Waleffe, and M. D. Graham, ''Toward a structural understanding of turbulent drag reduction: Nonlinear coherent states in viscoelastic shear flows,'' Phys. Rev. Lett. **89**, 208301 (2002).
[53]H. Massah, K. Kontomaris, W. R. Schowalter, and T. J. Hanratty, ''The configurations of a FENE bead-spring chain in transient rheological flows and in a turbulent flow,'' Phys. Fluids A **5**, 881 (1993).
[54]Q. Zhou and R. Akhavan, ''A comparison of FENE and FENE–P dumbbell and chain models in turbulent flow,'' J. Non-Newtonian Fluid Mech. **109**, 115 (2003).
[55]L. E. Wedgewood and R. B. Bird, ''From molecular models to the solution of flow problems,'' Ind. Eng. Chem. Res. **27**, 1313 (1988).
[56]R. B. Bird, C. F. Curtiss, R. C. Armstrong, and O. Hassager, *Dynamics of Polymeric Fluids* (Wiley, New York, 1987), Vol. 2.
[57]H. C. Öttinger, *Stochastic Processes in Polymeric Fluids* (Springer, Berlin, 1996).
[58]P. S. Doyle, E. S. G. Shaqfeh, G. H. McKinley, and S. H. Spiegelberg, ''Relaxation of dilute polymeric solutions following extensional flow,'' J. Non-Newtonian Fluid Mech. **76**, 79 (1998).
[59]R. Keunings, ''On the Peterline approximation for finitely extensible dumbbells,'' J. Non-Newtonian Fluid Mech. **68**, 85 (1997).
[60]R. G. Larson, ''The unravelling of a polymer chain in a strong extensional flow,'' Rheol. Acta **29**, 371 (1990).
[61]M. Laso and H. C. Öttinger, ''Calculation of viscoelastic flow using molecular models: The CONNFFESSIT approach,'' J. Non-Newtonian Fluid Mech. **47**, 1 (1993).
[62]M. A. Hulsen, A. P. G. van Heel, and B. H. A. A. van den Brule, ''Simulation of viscoelastic flows using Brownian configuration fields,'' J. Non-Newtonian Fluid Mech. **70**, 79 (1999).
[63]H. C. Öttinger, B. H. A. A. van den Brule, and M. A. Hulsen, ''Brownian configuration fields and variance reduced CONNFFESSIT,'' J. Non-Newtonian Fluid Mech. **70**, 255 (1997).
[64]J. Bonvin and M. Picasso, ''Variance reduction methods for CONNFFESSIT-like simulations,'' J. Non-Newtonian Fluid Mech. **84**, 191 (1999).
[65]P. Halin, G. Lielens, R. Keunings, and V. Legat, ''The Lagrangian particle method for macroscopic and micro-macro viscoelastic flow computations,'' J. Non-Newtonian Fluid Mech. **79**, 387 (1998).
[66]P. Wapperom, R. Keunings, and V. Legat, ''The backward-tracking Lagrangian particle method for transient viscoelastic flows,'' J. Non-Newtonian Fluid Mech. **91**, 273 (2000).
[67]M. Somasi, B. Khomami, N. J. Woo, J. S. Hur, and E. S. G. Shaqfeh, ''Brownian dynamics simulations of bead-rod and bead-spring chains: Numerical algorithms and coarse-graining issues,'' J. Non-Newtonian Fluid Mech. **108**, 227 (2002).
[68]K. D. Housiadas and A. N. Beris, ''Polymer-induced drag reduction: Effect of the variations in elasticity and inertia in turbulent viscoelastic channel flow,'' Phys. Fluids **15**, 2369 (2003).
[69]J. M. J. Den Toonder, A. A. Draad, G. D. C. Kuiken, and F. T. M. Nieuwstadt, ''Degradation effects of dilute polymer solutions on turbulent drag reduction in pipe flows,'' Appl. Sci. Res. **55**, 63 (1995).